國立交通大學

環境工程研究所

碩士論文

利用三辛基氧化膦包覆之二氧化鈦奈米晶粒

光降解內分泌干擾物質研究

Photoactivity of TOPO-capped TiO$_2$

nanocrystals for the degradation of endocrine disrupting

chemicals

研究生：羅品涵

指導教授：張淑閔　博士

中華民國九十七年九月

利用三辛基氧化膦包覆之二氧化鈦奈米晶粒光降解內分泌干擾物質研究

Photoactivity of TOPO-capped TiO$_2$ nanocrystals for the degradation of endocrine disrupting chemicals

研 究 生：羅品涵　　　　　　　Student: Pin-Han Lo

指導教授：張淑閔　　　　　　　Advisor: Sue-Ming Chang

國 立 交 通 大 學

環 境 工 程 研 究 所

碩 士 論 文

A Thesis

Submitted to Institute of Environmental Engineering

College of Engineering

National Chiao Tung University

In Partial Fulfillment of the Requirements

for the Degree of

Master In

Environmental Engineering

September 2008

Hsinchu, Taiwan, Republic of China

中 華 民 國 九 十 七 年 九 月

致謝

　　承蒙指導教授　張淑閔博士悉心指導，學習獨立思考與作研究應有的態度，自此學生向老師敬上最由衷的感謝之意。承蒙中央大學化材系陳郁文教授、清華大學醫環系董瑞安教授與孫毓璋教授，透過不同專業領域，提供許多寶貴的意見與討論，使本論文得以順利完成。

　　感謝傑耀學長、品欣學姐帶領我進入光催化世界與熟悉實驗室的學習環境，也讓我學到很多做人處事的道理；謝謝文彬學長無條件讓我使用 HPLC，教導我許多儀器分析上應有的知識；同窗好友維斯、精榮、阿苦、璧如、奕甫、嘉玲、俊竹等謝謝你們的陪伴，讓我在實驗苦悶時有人可以聊天與分享；與董老師實驗室的大家互相切磋，使我獲益良多；與學弟妹們彼此協助與討論，更是讓我的研究所生涯忙碌且充實。

　　感謝我的家人，因為你們的支持讓我沒有後顧之憂的完成論文，你們的微笑更是我繼續努力的原動力，我愛你們。最後要謝謝亮毅，在我無助時鼓勵我與包容我，我只能說有你真好。

　　僅以本文獻給所有關心我與曾經幫助過我的大家。

品涵　謹誌

中華民國 97 年 9 月

I

中文摘要

　　近年來，利用異相光催化反應分解內分泌干擾物質之議題備受矚目，其中，加強光觸媒中電子-電洞對轉移能力與促進污染物吸附於光觸媒上，於提升光催化反應過中污染物分解之效率有著十分重要的貢獻。本研究利用非水解性溶膠-凝膠法合成三辛基氧化膦包覆之二氧化鈦奈米晶粒 (TOPO-capped TiO_2)，並探討此光觸媒對三種不同親疏水性的環境荷爾蒙：酚($\log K_{ow} = 1.46$)、丙二酚($\log K_{ow} = 2.2$)與雌酮($\log K_{ow} = 3.13$)的光催化分解特性。結果證明有機修飾光觸媒對於內分泌干擾物質有優越的吸附能力，具有最高$\log K_{ow}$的雌酮於TOPO-capped TiO_2的分配係數最高為28.64 l/g，其次為丙二酚，其分配係數為 3.09 l/g，最低為酚，其分配係數為0.15 l/g，反之，P25對於水中內分泌干擾物質之分配能力則是十分微弱。光催化結果可以Langmuir-Hinshelwood反應動力式描述，發現TOPO-capped TiO_2 分解酚與丙二酚的速率分別優於商用觸媒P25的1.4和3.2倍;動力速率常數分別為$7.3×10^{-2}$和$1.4×10^{-1}$ ppm×g×min^{-1}×m^{-2}，為P25之0.9與2.7倍 ($8.2×10^{-2}$ 和$5.2×10^{-2}$ ppm×g×min^{-1}×m^{-2})，由於表面修飾的有機物會佔據二氧化鈦表面的活性位置，因此於降解酚的過程中，其速率常數略低於P25的表現，而TOPO-capped TiO_2對酚與丙二酚的吸附常數分別為$2.2×10^{-2}$ and $6.4×10^{-2}$ l/mg，為 P25 之 2.2 與 5.8 倍 ($1.0×10^{-2}$ and $1.1×10^{-2}$ l/mg)。由此可知 TOPO-capped TiO_2促進酚與丙二酚吸附於TiO_2，因此大幅提高其對環境荷

爾蒙降解能力。此外，EPR結果發現在TOPO-capped TiO$_2$系統中，光催化反應產生的氫氧自由基含量低，可知環境荷爾蒙主要利用電子電洞對進行直接光催化降解，且TOPO-capped TiO$_2$中捕捉住的電子與電洞量明顯大於P25，可知TOPO-capped TiO$_2$能有效抑制電荷再結合，以致於增進有效電荷利用率。總而言之，本研究合成有機物修飾之光觸媒具有良好有機物吸附能力與電子電洞對分離能力，因而大幅提升對環境荷爾蒙分解的光催化活性。與商用光觸媒 P25 相比，在處理不同親疏水性的環境汙染物上 TOPO-capped TiO$_2$對於催化極高疏水性的汙染物展現出優越的吸附與光催化能力，此種利用有機修飾光觸媒表面的材料為未來的環境汙染物降解議題提供了新的可行方案。

關鍵字： 異相光催化反應、內分泌干擾物質、三辛基氧化膦、分配能力、Langmuir-Hinshelwood、氫氧自由基

Abstract

Heterogeneous photocatalytic reaction for decomposition of endocrine disrupting chemicals (EDCs) has attracted much attention. The efficiency of photodecomposition is limited by the recombination of electrons and holes and the adsorption ability between catalysts and target compounds. In this study, modification of titanium dioxide (TiO_2) with trioctylphosphine oxide (TOPO) was prepared by a non-hydrolytic sol-gel method. The TOPO-capped TiO_2 exhibited high adsorption ability for EDCs. The partition coefficients of phenol, BPA and estrone in the presence TOPO-capped TiO_2 are 0.15, 3.09, and 28.64 l/g, respectively. In contrast, Degussa P25 adsorbs EDCs inefficiently. In the case of photocatalytic reaction, photocatalysis of EDCs follows Langmuir-Hinshelwood model. The initial rates for decomposition of phenol and bisphenol A (BPA) by TOPO-capped TiO_2 are 1.4 and 3.2 times, respectively, higher than those by Degussa P25. The kinetic rate constants of phenol and bisphenol A are 7.3×10^{-2} and 1.4×10^{-1} ppm×g×min^{-1}×m^{-2}, respectively, in the presence of TOPO-capped TiO_2, which are 0.9 and 2.7 times, respectively, higher than those in the P25 slurry (8.2×10^{-2} and 5.2×10^{-2} ppm×g×min^{-1}×m^{-2}). The smaller rate constant of TOPO-capped TiO_2 for decomposition of phenol is due to that the modifier occupied active sites. The adsorption coefficients of phenol and bisphenol A are 2.2×10^{-2} and 6.4×10^{-2} l/mg, respectively, in the presence of TOPO-capped TiO_2, which are 2.2 and 5.8 times, respectively, higher than those in the P25 slurry (1.0×10^{-2} and 1.1×10^{-2} l/mg). The photocatalytic mechanism of TOPO-capped TiO_2 mainly involves direct photodecomposition of these adsorbed EDCs by photo-generated charges rather by hydroxyl radicals which is normally occurred in the P25-based system. In addition, the intensity of trapped holes and electrons in TOPO-capped TiO_2 are much higher than that in P25. These results reveal that TOPO-capped TiO_2 improved interfacial charge transfer. In summary, the TOPO assists partition of EDCs onto the TiO_2 surface and facilitates interfacial charge transfer. These

contributions improve photocatalytic activity of TOPO-capped TiO_2.

Content Index

Figure Index

Table Index

Chapter 1. Introduction

1.1 Motivation

Over the past decades, considerable studies have been devoted on endocrine disrupting chemicals (EDCs). The presence of EDCs in the environment may disrupt the normal functions of the endocrine system in the wildlife and human health. There is sufficient evidence to believe that EDCs could impact: (a) mimicking and antagonizing of normal hormonal activity, (b) the effect of metabolism and abnormal of sexual development, (c) modifying hormone receptor levels. Some of these chemicals can cause the feminization of fish, sex transposition of wildlife, and hormone-related cancers in humans.[1-5] Environmental scientists concern to develop the effective treatment method for removal of EDCs.

Many researches showed that the traditional water and wastewater treatment plant (WWTP) is not efficient for removing EDCs. Wasteroff and Nakada et al. reported that combination of 5 mg/l of activated carbon, ozonation and sand filtration in the WTP can improve the removal efficiency.[1, 6, 7] Moreover, TiO_2-based photocatalysis attracts much attention on elimination of the hazardous chemical wastes because it is non-toxicity, low cost, high reactivity, photochemical stability, suitable excited energy.[8-10] Ohko et al.[11] decomposed BPA using TiO_2 and found that the photocatalysis reduced the estrogenic activity without generating secondary pollutants. In recent years, surface modification of TiO_2 surface with surfactants has proved to have advantage to enhance the photoactivity. Kurinobu et al.[12] decomposed methylene blue, red basic dye, blue basic dye, nonylphenol, and octylphenol by adsorption and photocatalytic reaction with magnetic photocatalyst. Kohtani et al.[13] enhanced the adsorption capacity and photocatalytic efficiency of 4-n-octylphenol by Ag loaded on $BiVO_4$ photocatalyst. Silica-immobilized polyoxometalate can photodecompose and mineralize of 4-chlorophenol.[14] Alkyl-grafted TiO_2-MCM-41 can

degrade the 4-nonylphenol polyethoxylate efficiently.[15]   The most likely explanations of the high photocatalytic efficiency of the modified TiO$_2$ are (a) to increase the adsorption ability of TiO$_2$ surface;[16-20] (b) to maintain well dispersed TiO$_2$ nanoparticles;[21] (c) to inhibit charge recombination;[22-24] (d) to cause the red shift of photocatalysts.[20, 22, 25, 26]

Chang and Doong[27] have successfully synthesized the surface-modified Zr-doped TiO$_2$ nanoparticles by a non-hydrolytic sol-gel process (NHSG) and demonstrated high photocatalytic activity for decomposition of RhB.   The NHSG process can obtain the well crystalline phase, controlled particle size and well distribution of metal oxides.[28]   However, there are few studies discussing the photocatalytic activity with respect to the adsorption behavior induced by hydrophobic/hydrophilic charaters between EDCs and the modified TiO$_2$ so far.   In addition, the effect of the surface modifier, TOPO, on the inhibition of charge recombination is not clear yet.

1.2   Objectives

This research have successfully synthesized the trioctylphosphine oxide (TOPO) modified titania via NHSG process.   This study presents the EDCs partition and photocatalysis kinetics on TOPO-capped TiO$_2$ and compared with Degussa P25. (Figure 1-1) Thus, the mechanism of photocatalysis by TOPO-capped TiO$_2$ illumination needs to be identified.   The dominant rate-limiting step of the photodecomposition is investigated in this study.   Moreover, many organic chemical-modification of TiO$_2$ surface will be damaged after photocatalysis.   Then, calculate and compare the surface quantities ratio of carbon and phosphorous atoms before and after photocatalysis.
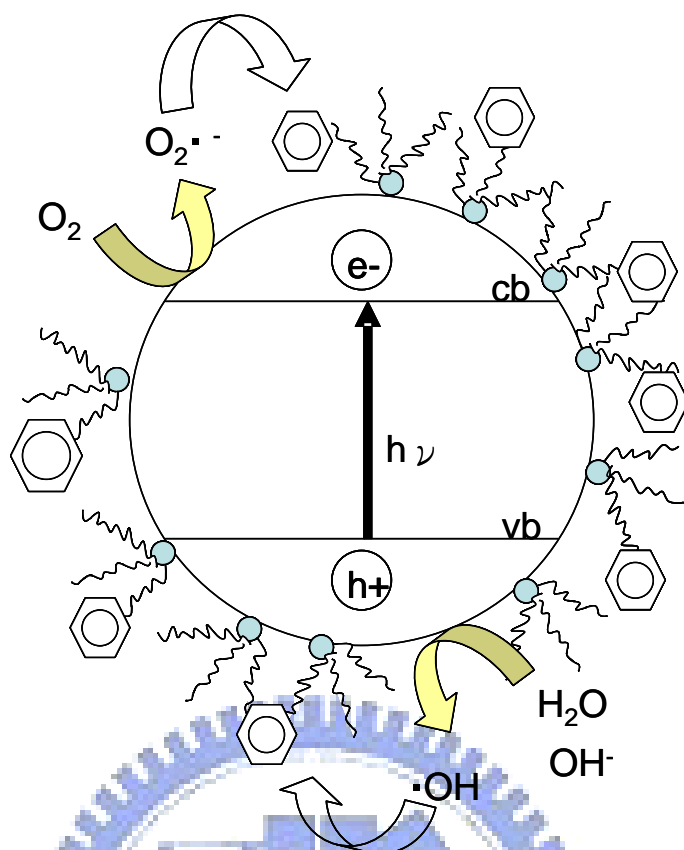
Figure 1-1　Photocatalytic reaction between TiO_2 and EDCs.
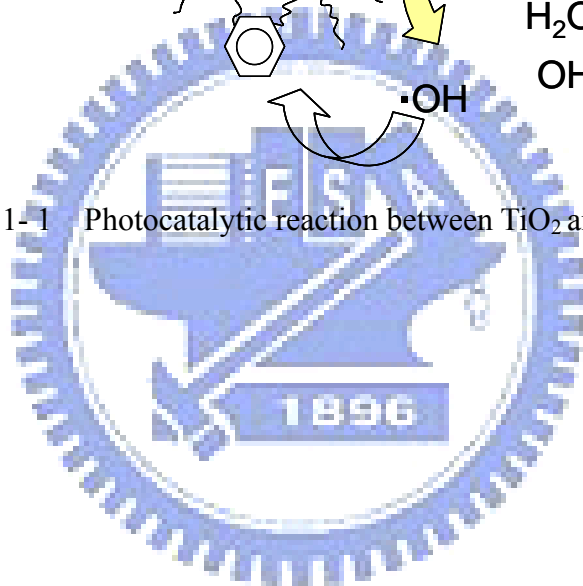
Chapter 2.   Background and Introduction

2.1   Photocatalysis

2.1.1   Principle of photocatalysis

The treatment technique of waste water and air by semiconductor photocatalysis is a new milestone in this century.   They aim to enhance the efficiency of treatment of environmental pollutants.   We can use metal oxides (TiO_2, ZnO, ZrO_2 and CeO_2) and metal chalconides (CdS, ZnS) as our photocatalysts to degrade the organic compounds in waste water by photocatalytic degradation processes.[10, 14]   The most widely used photocatalyst, TiO_2, has high photo-efficiency, low cost and environmentally friendly.[9, 29]   Recently, photocatalysis of TiO_2 materials have been focused on the purification of air and water, sterilizing and offensive odor.[30]

When the energy of photon is equal to or higher than the band gap energy of semiconductors, the semiconductors will photogenerate the electron and hole pairs. Electrons are excited from the valence band of the irradiated particles to its conduction band with simultaneously leaving holes in the former.   The electron and hole can recombine on the surface or in the bulk of the catalyst in few nanoseconds.   Furthermore, the generated electron and hole can easily and quickly migrate to the surface.   In this photocatalytic (redox) reaction, these charges can directly react with organic pollutants adsorbed or close to the surface of the particles.   An electron transfer proceeds towards acceptor molecules, whereas positive holes are transferred to donor molecules.   Holes in the valence band may react with OH^- and H_2O molecules adsorbed at the semiconductor surface to produce hydroxyl radicals ($\cdot OH$).   In addition, the conduction band is negative enough to reduce adsorbed oxygen to form superoxide radicals ($O_2\cdot^-$), that can further disproportionate to form $\cdot OH$ through various pathways.   The redox reactions resulting from the hole-electron pairs at the surface of the semiconductor can then convert organic compounds into oxidized or reduced products.

Finally, the mineralization of organic pollutants to CO_2, H_2O and mineral acid is achieved by radicals attack. (Figure 2-1)[8, 10, 31-34].
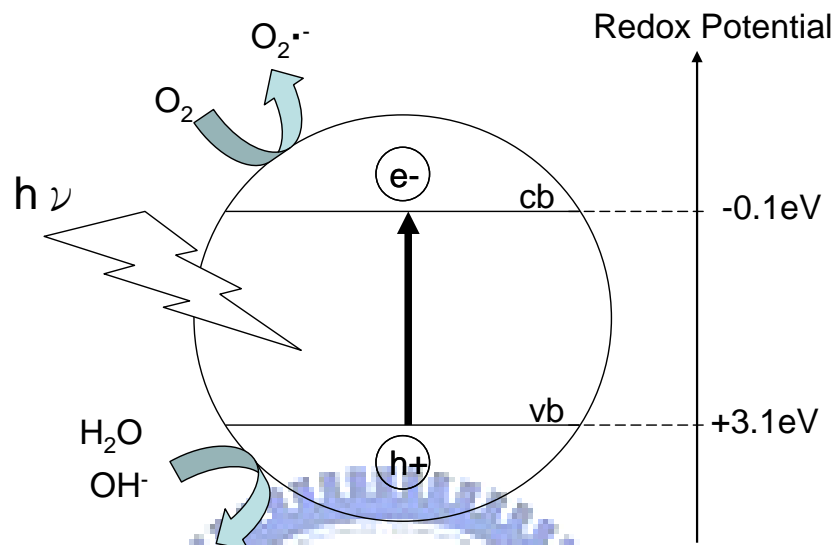
Figure 2- 1   Reaction diagram of photocatalysis at a semiconductor by illumination.

The steps representing the proposed mechanisms can be expressed by following set of simplified equations:[31]

Band gap illumination (hν) onto a photocatalyst causes the electronic transitions.

$$TiO_2 \xrightarrow{\ h\nu\ } TiO_2 \ (e^- \text{ and } h^+ \text{ pairs})$$

Photogenerated holes oxidize the adsorbed water and OH^-.

$$h^+ + H_2O_{ads} \rightarrow \ \cdot OH_{\ ads} + H^+$$

$$h^+ + OH^-_{\ ads} \rightarrow \ \cdot OH_{\ ads}$$
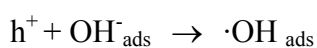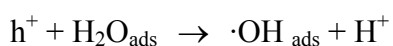
Photogenerated electrons react with adsorbed O_2.

$$e^- + O_{2ads} + H^+ \rightarrow HO_2 \cdot \ \Leftrightarrow \ O_2 \cdot^- + H^+$$

$$2HO_2 \cdot \ \rightarrow H_2O_2 + O_2$$

$$H_2O_2 + O_2 \cdot^- \rightarrow \cdot OH + O_2 + OH^-$$

$$H_2O_2 + h\nu \rightarrow 2 \cdot OH$$

$$H_2O_2 + e^- \rightarrow \cdot OH + OH^-$$
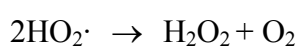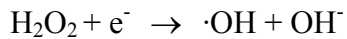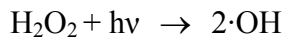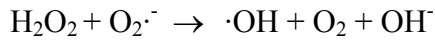
The overall photocatalytic reactions.

$$\text{Organic pollutants} + O_2 \xrightarrow{\text{photocatalysis}} CO_2 + H_2O + \text{mineral acid}$$
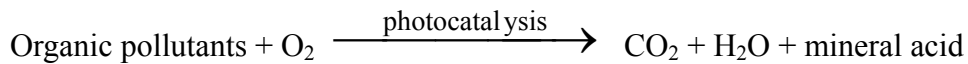
2.1.2 Photocatalysts

Numerous photocatalysts, including TiO_2, ZnO, ZnS, WO_3, CdS and SnO_2, have recently been investigated for the destruction of organic containments in global water and air pollution,. Figure 2-2 shows the band edge position of various semiconductors. From the available semiconductors, TiO_2 has received much attention and been frequently utilized due to their exceptional electronic and optical properties, high photocatalytic activity, chemical stability, non-toxicity, low cost and suitable band gap energy with wavelength less than 400 nm.[8-10]

TiO_2 has three kinds of crystal phases, anatase, rutile and brookite. The commonly used phases are anatase and rutile, as displayed in Figure 2-3. Anatase is a metastable phase which can transfer to rutile phase above 550 °C. The band gap energies of anatase and rutile are 3.2 eV and 3.0 eV respectively. Generally, anatase has several advantages in the photocatalytic region, including low h^+-e^- recombination possibility, more surface adsorbed water and hydroxyl groups, larger surface area than rutile, which can enhance the photocatalytic efficiency, obviously. Comparatively, rutile is less active. However, the Germany Company Degussa, they mixed 80% anatase and 20% rutile to produce P25, are contributing to excellent photocatalytic activity. Nowadays, P25 is a mostly widely used photocatalyst. For P25, it has band gap around -0.3 eV to +2.9 eV.[9, 31, 32, 35]
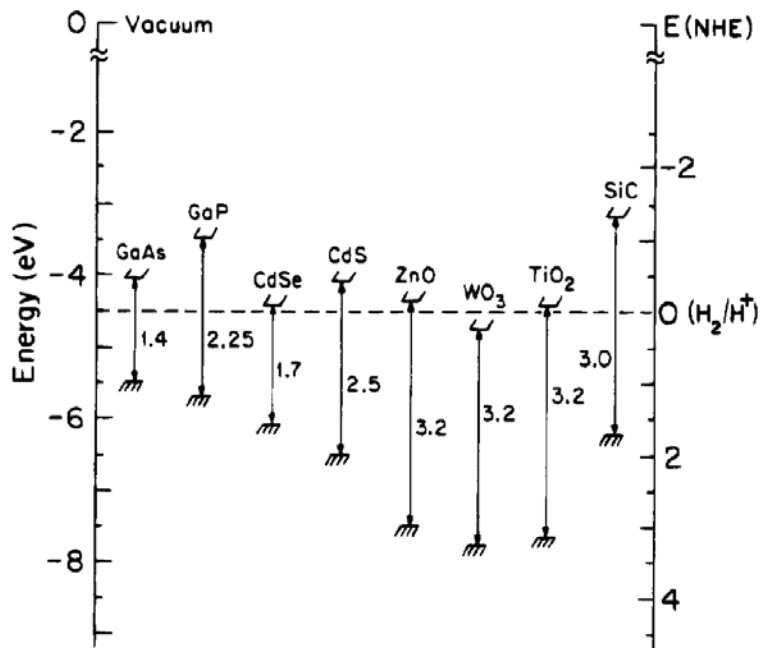
Figure 2- 2   The redox potentials of various semiconductors related to the energy levels.[32]
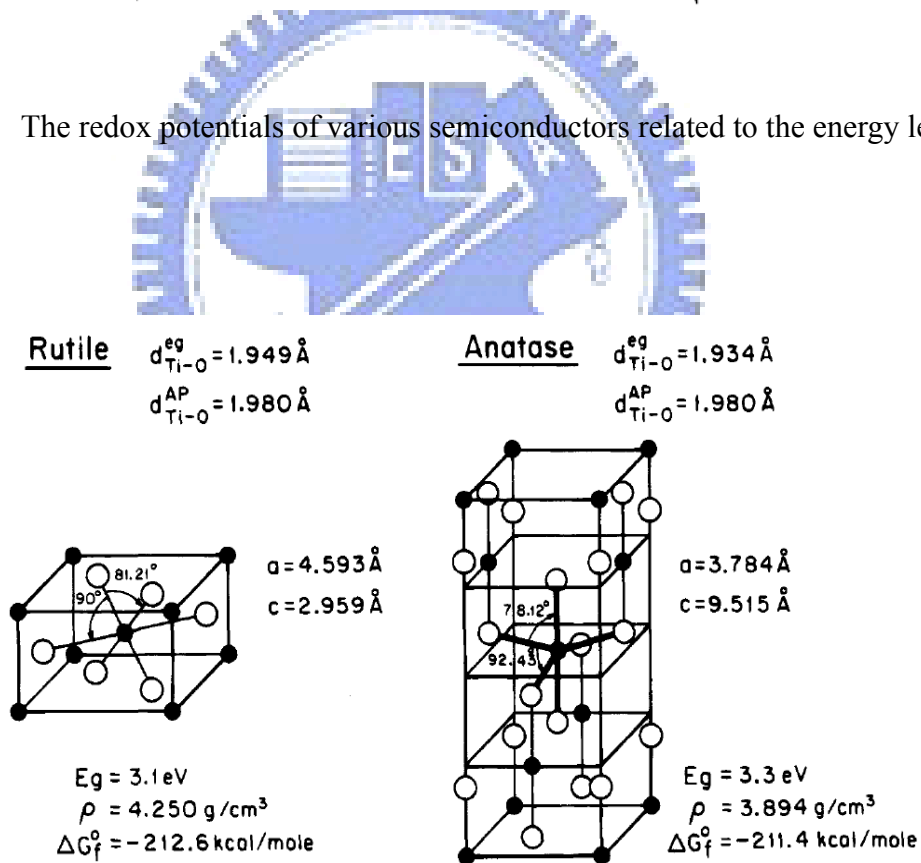
Figure 2- 3   Structure of rutile and anatase TiO_2.[32]

2.2 Sol-gel method

2.2.1 Hydrolytical Sol-Gel process

The sol-gel method is a versatile process and comprehensively utilized in making various nanostructure materials. In a typical synthetic procedure, the colloidal sol suspension is formed from the hydrolysis and polymerization reaction of the precursors which usually are metal salts and metal alkoxides. In general, sol-gel method exhibits a distinct advantage in several folds: (1) the process can be carried out at room temperature (2) easily control the morphology of the materials (3) highly regular and homogeneous materials (4) low costs. As a result of above advantages, the sol-gel can be one of the candidates of preparing nanostructure materials.

Figure 2-4 represents the typical process of sol-gel method as follows. First of all, the precursors dissolving in water rapidly hydrolyze and condense subsequently. Eventually, the polymerization and gelation of the condensed intermediates lead to the formation of the colloidal gel.[36-38]
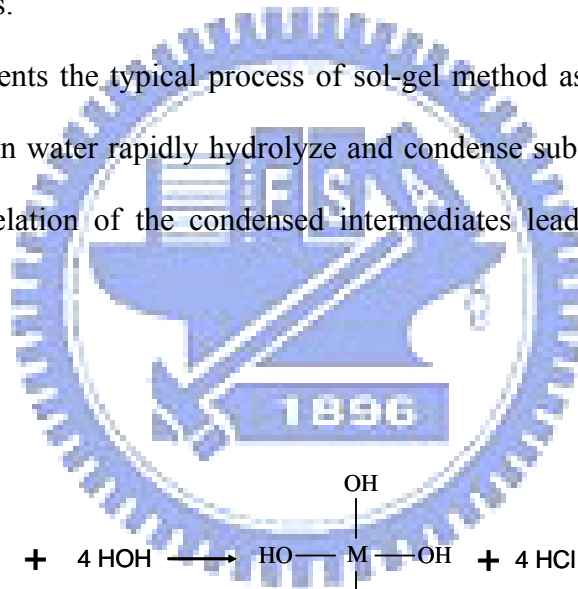
Hydrolysis
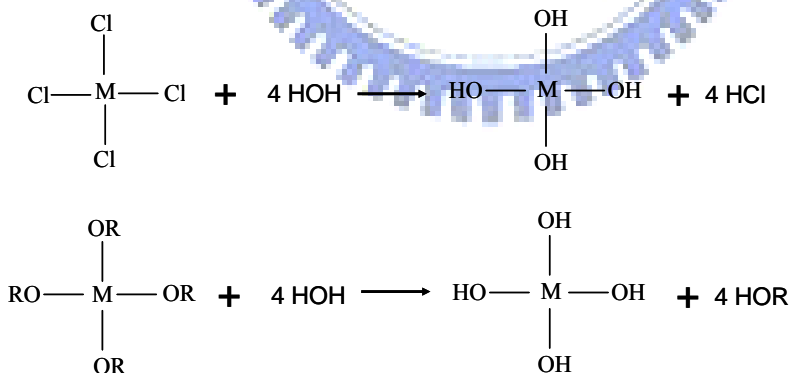
Polycondensation
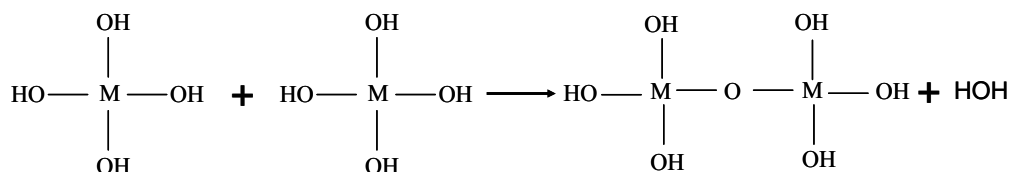
Gelation
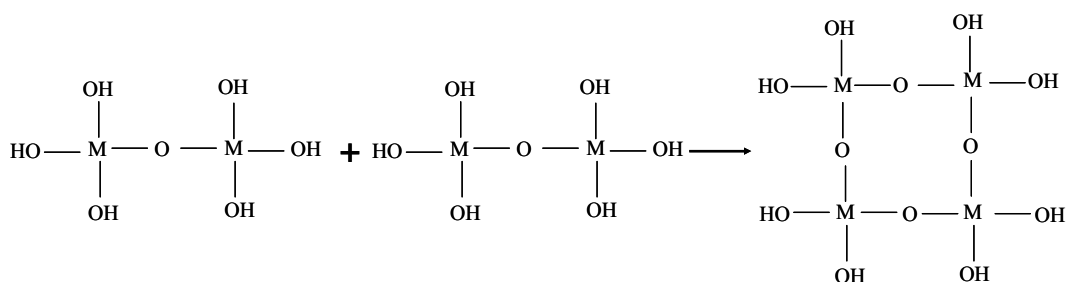
Figure 2- 4   Hydrolytic sol-gel process.

2.2.2   Non-Hydrolytic Sol-Gel process

Using non-hydrolytic sol-gel method can get the homogeneous multicomponent oxides, such as Al_2TiO_5 and $ZrTiO_4$.   Moreover, the organic and inorganic molecules can be hybridized with NHSG method.[37-43]

The considerable purpose of non-hydrolytic sol-gel method is devoted to synthesize the dispersible TiO_2 nanoparticles.   Figure 2-5 shows the synthesis mechanism of TiO_2 with NHSG process.   The major reactions under 80 to 150 °C could be thermal condensation or etherolysis.   Thermal condensation occurs between metal chlorides and metal alkoxides, more exactly, the lone pair of electrons from alkoxyl oxygen will move to metal center, and followed by the cleavage of halide and alkyl groups.   On the other hand, etherolysis forms the alkoxide function groups between metal chlorides and ether.   Both reactions form metal oxide and alkyl halides.   If the temperature is low (ambient temperature), ligand exchange between metal chlorides and metal alkoxides will take place. [37, 39, 40, 42-44]

However, there are several differences between conventional sol-gel process and non-hydrolytic sol-gel route.   Two reasonable consider seem to be helpful to elucidate: (a) homogeneous metal oxide can be synthesized at low temperature; (b) increasing the thermal stability; (c) enhancing the crystalline growth; (d) to control the crystalline size; (e) to prepare the dispersible powders.[37, 39, 40, 43]

Condensation

$$MCl_n + M(OR)_n \longrightarrow 2\ MO_{n/2} + n\ R\text{-}Cl$$

$$M\text{-}OR + M\text{-}X \rightleftharpoons \quad \longrightarrow \quad M\text{-}O\text{-}M + R\text{-}X$$

Etherolysis

$$\equiv M\text{-}Cl + R\text{-}O\text{-}R \longrightarrow\ \equiv M\text{-}OR + R\text{-}Cl$$

$$MCl_n + n/2\ R\text{-}O\text{-}R \longrightarrow MO_{n/2} + n\ R\text{-}Cl$$
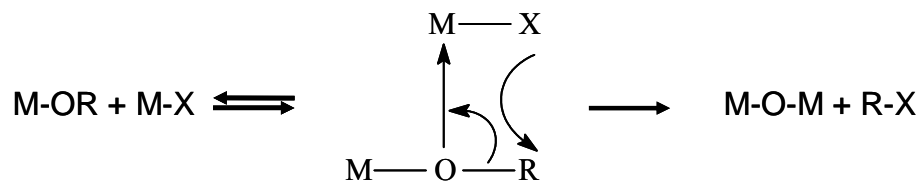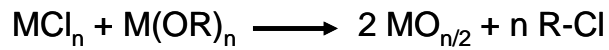
Ligand Exchange (redistribution)

$$\equiv M\text{-}Cl + \equiv M\text{-}OR \longrightarrow\ \equiv M\text{-}OR + \equiv M\text{-}Cl$$
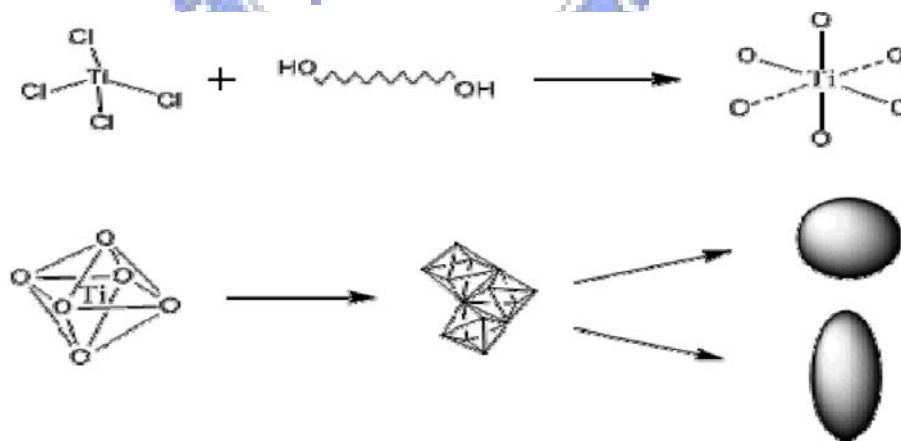
Figure 2- 5   Synthesis mechanism of TiO_2 by NHSG.[45]

2.3 Surface Modification

In the recent years, TiO_2 has been the most extensive and intensive investigated nanomaterials, because it can eliminate pollutants chemicals in air, solid and water environments. Large effort has been devoted to improve the photocatalytic activity, determine their chemical composition, surface characteristics, and physical properties. Many efforts have been focused on surface modification technologies in order to enhance photocatalytic efficiency and perform widely applications, including doping impurities, coupling with metal oxide, and coating with organic or inorganic compounds and treating TiO_2 with acid.

Several researches may consider the purposes of the modified TiO_2 under the following heads: (a) to increase the surface coverage of target compounds onto TiO_2 surface;[16-20] (b) to avoid agglomeration of TiO_2 powders;[21] (c) to inhibit the recombination of electrons and holes;[22-24] (d) to expend the wavelength response range;[20, 22, 25, 26] (e) to control the structural properties,[46-49] and (f) to greater control the resulting photoproducts. For these reasons, surface modifier systematically shows the important role in the photocatalytic reaction. Table 2-1 summarizes using organic molecule modified TiO_2 surface has proved highly effective in the photodegradation ability of target compounds.

Compared with the unmodified TiO_2, surface modification of TiO_2 by pseudo-boehmite and salicylic acid proved to be the higher amount of bromate and 4-chlorophenol adsorbed than unmodified TiO_2. Subsequently, the degradation efficiencies by TiO_2 could be enhanced after surface modification.[18, 20] Surfactant cover can make TiO_2 surface hydrophobic and enhance the adsorption of hydrophobic organic compounds (HOCs) on the surface. Yuan and Ravikrishna et al. found that fluorocarbon-based surfactant, potassium perfluorooctylsulfonate (PFOS) on to TiO_2 surface acts to promote the adsorption and degradation of 1,2-dichlorobenzene (DCB). However, sodium dodecylsulfate (SDS) may competitively decomposed with DCB, lead to decreasing the photocatalytic ability.[19] Yu et al. were covered thin layer of carbon on ST-01 particles, namely carbon-coated anatase.

After 900 °C treated catalysts, pyrone-like basic structures have been formed on the surface and performed the higher phenol adsorption and photodecomposition.[17]

Surface modification method of titanium dioxide (TiO_2) can prevent irreversible agglomeration, and obtain the well-dispersed TiO_2 nanoparticles. When the calcination temperature up to 760 °C, surface modifier, diethylene glycol monomethyl ether, suppressed the sintered nanoparticles and the particle size maintained lower than 50 nm.[21]

On the other hand, more and more studies have been published that organic modification on TiO_2 surface can expand the absorption wavelength into visible region.[20, 22, 25, 26]   For example, TiO_2 modified with ascorbic acid, photoinduced electrons can migrate from modifier to the conduction band of TiO_2 by visible light illumination. This photocatalyst can inhibit the charge pair recombination, and then enhance the methyl orange photocatalytic decolorization rate.[22, 25]   The -NCO groups of tolylene diisocyanate (TDI) react with the surface hydroxyls of TiO_2 to form TDI-modified TiO_2 nanomaterials. The photocatalytic efficiency increased with increasing the TDI content.[26]

Korosi et al. founded that phosphoric acid modifier affects the surface area, pore volume and pore size of titanium dioxide materials.[46, 47] PO_4^{3-} ions are bonded to the surface of titanium dioxide, and the surface hydroxyl groups may react with the phosphate ions, leading to cross-linking. The phosphorus was chelated to the framework of TiO_2 particles and formed Ti-O-P bonds. Additionally, phosphate ions incorporated with TiO_2 has high thermal stability at high temperature treatment. Moreover, thermal stability plays an important role in the crystalline growth during the calcination process which can effectively prevent condensation and inhibit the growth of crystals.[48]   The surface area and pore volume of phosphate-modified TiO_2 particles increased and crystalline size decreases with increasing phosphate content. Quantum crystal TiO_2 with intrinsically wider range of adsorption edge can be observed after phosphoric acid treatment. However, the larger specific surface area may promote the photodegradation of target molecules.[46, 47, 49]

Table 2- 1   Surface modification of TiO$_2$ and its advantages.

Advantages	Surface modifier	Objective	Reference
Adsorption	Pseudo-boehmite	Increase in the amount of adsorbed BrO$_3^-$ on the photocatalyst surface.	Noguchi et al.[18]
	Salicylic acid	Improve the surface coverage of 4-nitrophenol.	Li et al.[20]
	3-aminopropyl-triethoxysilane	Adsorption of C.I. Acid Orange 7 on TiO$_2$ surface.	Andrzejewska et al.[16]
	Carbon	Adsorption of phenol onto carbon layer coating anatase particles.	Tryba et al.[17]
	PFOS and SDS	Enhance 1,2-dichlorobenzene adsorption and degradation.	Yuan et al.[19]
	Arginine	Enhance nitrobenzene adsorption and decomposition.	Makarova et al.[24]
Charge recombination	Trifluoroacetic acid	Reduce the electron-hole recombination.	Yu et al.[23]
	Ascorbic acid	Enhance the generation of superoxidesand and occur on the surface modified TiO$_2$ with AA.	Ou et al.[22]
	Arginine	Facilitate the transfer of photogenerated electrons from the TiO$_2$ conduction band to the adsorbed nitrobenzene.	Makarova et al.[24]

Dispersed capacity	Diethylene glycol monomethyl ether		Simakov et al.[21]
Red shift	Ascorbic acid	The incident-photon-to-current efficiency presents at 415 nm.	Xagas et al.[25]
	Ascorbic acid	Enhancing utilization of the solar spectrum.	Ou et al.[22]
	Tolylene diisocyanate (TDI)	Under visible light irradiation.	Jiang et al.[26]
	Salicylic acid	Absorption in the region from 320 to 420 nm.	Li et al.[20]
Thermal stability	Phosphoric acid	The specific surface area increases with increasing phosphate content at a given calcination temperature.	Korosi et al.[46-49]
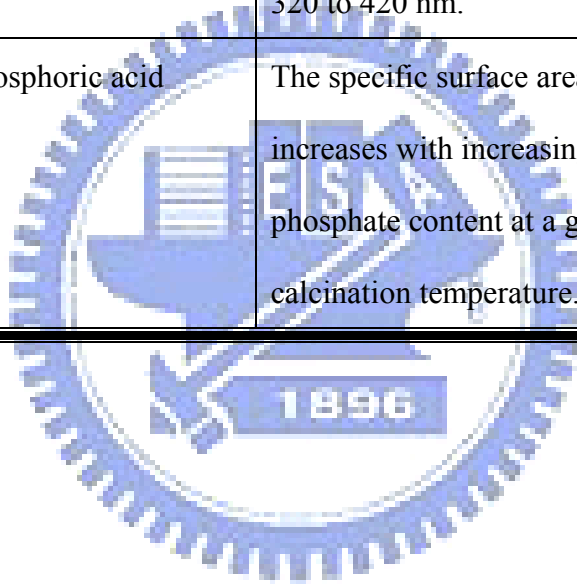
2.4 Endocrine Disrupting Chemicals

Several types of environmental pollutants referred to as endocrine disrupting chemicals (EDCs) at listed by Environmental Agency of Japan. A wide range of pollutants present in the industrial effluent containing EDCs, such as pulp and paper mill, dye industry, pharmaceuticals, and detergent metabolites has been detected in the rain, lakes, ground water, coastal zones and ocean. The presences of EDCs are accumulated in rivers and oceans, and possible impact on wildlife and human health even at low concentration. These pollutants cause the mimicking and antagonizing of normal hormonal activity, the effect of metabolism and abnormal of sexual development. Moreover, the endocrine effects for humans are including decrease the sperm count and quality in male and increase frequency of breast cancer in women.[2, 4, 5, 7, 50-53]

For example, 1950s in Great Lakes in North America, researchers found 100% of thyroid enlargement in 2-4 years old salmon and high prevalence of acceleration of sexual maturation.[4] Female mosquito fish in the paper mill effluent became to male specific gonadopodia and other species.[54]

In this research, we choose three kinds of endocrine disrupting chemicals (EDCs) as our target compounds, phenol, BPA and estrone. Recently, BPA is widely applied in various polycarbonate plastics, poly(vinylchloride) (PVC), epoxy resins such as the inner coating of food cans, powder paints, plastic containers, dental fillings and baby bottles. The harmful compounds, BPA, can be released during autoclaving and lead to human exposure to BPA. Furthermore, EDCs can accumulate in the surrounding ecosystem, and the effective treatment technologies of EDCs are required urgently.[51, 55-58]

The limitations of EDCs discharge in the industrial effluent and municipal sewage have been monitored and controlled. In America, the scientists have confirmed that EDCs may disrupt endocrine and affect estrogenic activity. The government order to forbid using pesticides containing lindane. In Europe, they also forbid using pesticides and cleansers contained environmental hormones. In Japan, they don't use the plastics manufacture by

polyvinyl chloride (PVC).

2.5   Photocatalytic Degradation for EDCs

Many pollutants have been used in industrial advances and these may cause effects severely to environmental living organisms.   Recently, the use of heterogeneous photocatalytic reaction of organic pollutants is a promising and emerging treatment for effluent decontamination since the conventional biological treatment processes are not effective.   Photocatalytic processes take place when the semiconductor adsorbs enough energy to excite electrons and holes.   Then, the formation of ·OH radicals behave strong oxidants, which can decompose pollutants into non-toxic then mineralizes to carbon dioxide finally.[55, 59-61]

2.5.1   Photocatalytic degradation technology for phenol

Table 2-2 shows the photodegradation of phenol using modified TiO_2.   Several tradition ions modified TiO_2 were observed to encourage the photoactivity of phenol in water.[59, 62, 63]   For examples, surface modification methods including platinum doping and photodeposition of metal silver on TiO_2 can act as trapping sites to efficiently suppress the charge recombination and increase the photoactivity.[59, 64]   Using iron as dopant can increase photocatalytic degradation of phenol in domestic water suspensions.[62, 63]   The co-doped Zr and Fe TiO_2 samples enhance thermal stability and reduce the crystalline size after annealing. Moreover, the dopants arrange randomly on the TiO_2 surface, the band poison can separate the charge carrier significantly.[63]

Further, the photo-Fenton reactions is meaning that H_2O_2 and Fe^{2+} react to form ·OH, OH^- and Fe^{3+}.   Then, the photoexcited electron affords to Fe^{3+} to become Fe^{2+} from semiconductor, and this process can start again.[65, 66]   Tryba et al. have been found that the addition of H_2O_2 in the photocatalytic system, the Fe-modified carbon-coated TiO_2 and calcined at 400 °C can enhance the decomposition rate of phenol.[66]   During calcination, the

sulfuric and phosphoric acid pre-treatment TiO_2 has higher thermal stability lead to hinder anatase-rutile conversion and relatively high surface area.[67]

Figure 2-6 suggests the photocatalytic decomposition pathway of phenol and generated intermediate products.   Under photocatalysis, the ·OH are a powerful oxidant to attack phenol, then the ring has been opened, causing hydroquinone (HQ), benzoquinone, catechol (CC) and some organic acids.   And, finally the complete mineralization is achieved to CO_2 and water.[29, 68]
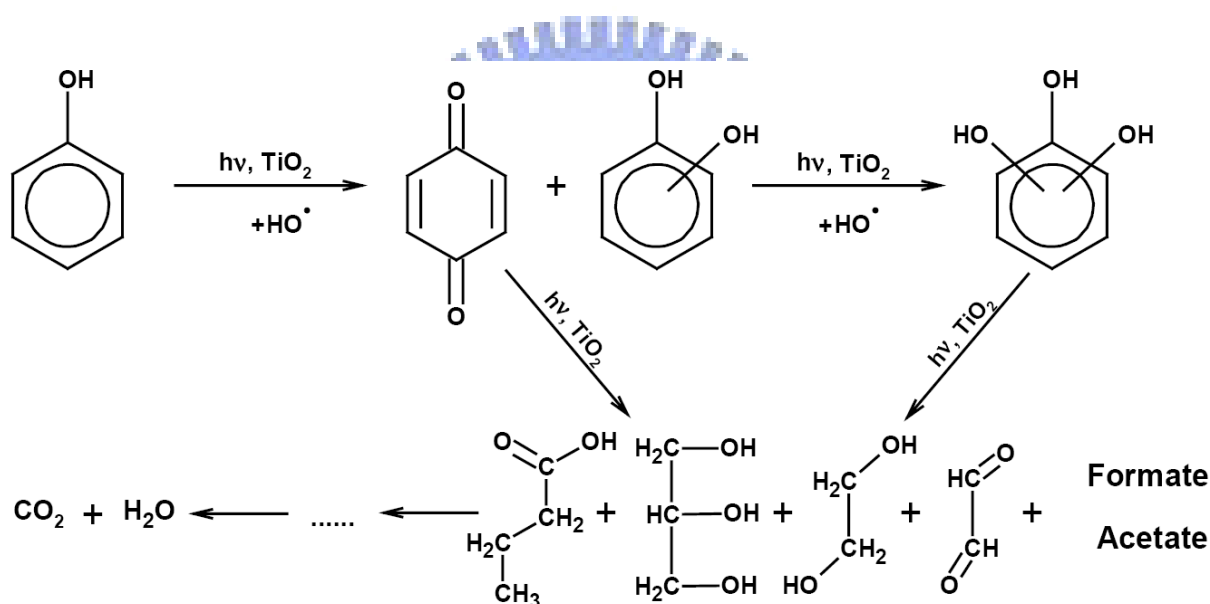
Figure 2- 6   Photocatalysis decomposition pathway of phenol.[68]

Table 2- 2   Photocatalytic degradation of phenol with modified TiO_2.

Method	Materials	Optimal condition	Motivation	Reference
Doping	Fe	$Fe_{0.005}Ti_{0.995}O_2$	Red shift, Photoactivity	Nahar et al.[62]
	Zr (II) + Fe(III)	0.5 mol% Zn + 1 mol% Fe	Photoactivity	Yuan et al.[63]
Deposition	Silver	0.5 wt %	Photoactivity	Dobosz et al.[64]
	Platinum	0.1 wt % Pt/P25 and 1 wt % Pt/HK	Photoactivity	Sun et al.[59]
Acid pre-treatment	Nitrate, Sulfate and Phosphate	Sulfate	Thermal stability	Colon et al.[67]
Coating	Fe and Carbon	Fe-modified carbon-coated TiO_2 and calcined at 400 °C in H_2O_2 system.	Adsorption, Photoactivity	Tryba et al.[66]
	Fe and Carbon	$TiO_2 : FeC_2O_4 = 10:1$ and heating at 550 °C for 3 h in H_2O_2 system	Photoactivity	Tryba et al.[65]

2.5.2 Photocatalytic degradation technology for BPA

Many researches have been reported to improve the photocatalytic efficiency of BPA (Table 2-3). The following serves as several examples:

At acid situation (pH 3), the BPA molecules are the un-ionized form and the TiO_2 surface exhibits positive charge. BPA could be more easily adsorbed onto TiO_2 surface and could be decompose by adsorbed radicals. On the contrary, even, the TiO_2 surface concentration of [·OH] increases with $[H^+]$ concentration increasing in the alkaline situation. But, BPA can't be adsorbed on the catalyst surface and attacked by the surface ·OH. Therefore, in the acidic condition, the photoefficiency of optimum platinum loading (between 0.2 wt % and 1.0 wt %) is 3-6 times faster than that of bare TiO_2.[55, 60]

Impurities other than titanium were mostly used to dope into the lattice of TiO_2 to increase the photoactivity. Doping metals such as Mg^{2+} and Ba^{2+} can replace the Ti^{4+} space, and provide an additional energy level. Mg^{2+} and Ba^{2+} loadings can decrease the particle size and enhance the adsorption of BPA on the TiO_2 surface. However, according to the quantum size effect, the entry of Mg^{2+} in the crystalline structure suppresses the crystal growth and consequently increases the photoinduced wavelength. Besides, the Ba^{2+} ionic radius (1.49 Å) is larger than Ti^{4+}, the $BaCO_3$ on the external surface of TiO_2 is established. Further, the carbonate layer can adsorb BPA via hydrogen bonds and lead to higher adsorption ability. It's clearly explained that photocatalytic degradation of BPA with Mg^{2+} and Ba^{2+} doped TiO_2 nanoparticles has higher efficiency than both pure TiO_2 and Degussa P25.[69]

Several novel metals and transition metals (Au, Ag and Pt) have been deposited on the surface of TiO_2 powder can induce Schottky barrier effect to help the electron redistribution and prevent the electron-hole recombination rate. It can be expected to be an effective treatment technology for removing BPA from waste water.[61, 70-72]

Photo-fenton process for wastewater treatment has been developed for the degradation of BPA by mixing Fe^{2+} and H_2O_2.[73] Ioan et al. found that sono-fenton can produce

more ·OH radicals in the ultrasonic physical and chemical processes, then enhance the photocatalysis of BPA.[74]

During photooxidation of BPA, the intermediates including 4-isopropylphenol ($m/z = 135$), 3-(4-hydroxyphenyl)-3-methyl-2-oxobutanoic acid (HPMOBA, $m/z = 208$), 4-vinylphenol (VP, $m/z = 134$) and 4-hydroxyacetophenone (HAP, $m/z = 136$) can be identified by LC/MS and summarized the photodegradation mechanism in Figure 2-7.   Then, the formic acid and acetic acid were produced and CO_2 gas evolution finally.[11, 58]
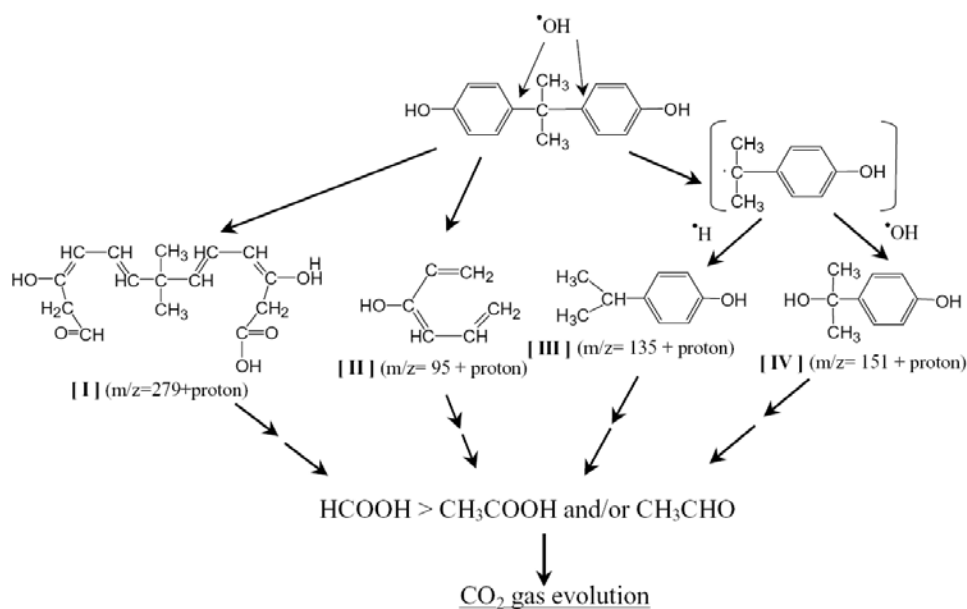
Figure 2- 7   Photocatalysis decomposition pathway of BPA.[58]

Table 2- 3   Photocatalytic degradation of BPA with TiO_2.

	Methods		Reference
Degradation Method	Photocatalysis	TiO_2 coated on glass tubes	Lee et al.[50]
		Photodeposition of silver and platinum	Coleman et al.[70]
		Au-TiO_2/ITO	Li et al.[71]
		Pt-loaded TiO_2	Zhang et al.[60, 61]
		Mg^{2+} and Ba^{2+} doped TiO_2	Venkatachalam et al.[69]
		Addition of H_2O_2 in Au-TiO_2/Ti system (electron scavengers)	Xie et al.[72]
	Addition of β-cyclodextrin in reaction system (adsorption ability)		Wang et al.[55]
	Fenton-process		Katsumata et al.[73] Ioan et al.[74]
	Ultrasonic destruction		Gultekin et al.[75]

2.5.3   Photocatalytic degradation for estrone

The estrone (E1) and 17β-estradiol (E2) were affected by several parameters such as initial concentration of pollutants, pH value, ionic strength and the presence of humic acid and H_2O_2 obviously.[76, 77]   Humic acid can competitively adsorb on the surface of TiO_2, leading to accelerate of the electronic energy transfer from humic acid to E1 and E2. Hydroxyl radicals attack, photogenerated electrons and holes attack directly will be affected the photoefficiency, depending on the initial pH value.[78]   They calculated that E1 and E2 have the best performance at optimum pH value of 7.6.[77]

Estradiol (E2), estrone (E1) and estrogen conjugates (estradiol-3-glucuronide ($E_2$3G), estradiol -17-glucuronide ($E_2$17G), estrone-glucuronide (E_1G), estrone-sulfate (E_1S) and E_3 3-sulfate 16-glucuronide ($E_3$3S16G)) were subjected to photocatalytic degradation by TiO_2 immobilized on glass beads as a photocatalyst.   The glucuronic acid moiety on the skeleton and sulfonic acid moiety at the phenolic hydroxy group may accelerate the degradation rate. Thus, $E_2$3G, $E_2$17G, E_1G and $E_3$3S16G are degraded faster than E_2 and E_1.[79]

After 7 minutes photocatalysis, the photodegradation efficiency of estrone reached 50% and 100% removal within 1 hour.   Under UVA illumination for 360 minutes, estrone has been photolyzed totally.[80]

Chapter 3.   Experimental Materials and Methods

3.1   Chemicals

Titanium isopropoxide (TTIP, $Ti(OC_3H_7)_4$, 98+ %) and titanium chloride ($TiCl_4$, 99.9 %) were used as the titanium precursors and obtained from Acros Organics and Showa Chemicals, respectively.   Trioctylphosphine oxide (TOPO, $[CH_3(CH_2)_7]_3PO$, 99 %, reagent plus; melting point: 50-52 °C) is supplied by Strem Chemicals.   TOPO is moisture sensitive and need to be stored in a glove box.

Three kinds of endocrine disrupting chemicals including phenol (99.5 %, Riedel-de Haen Company), bisphenol A (BPA, 99+ %, Sigma-Aldrich Chemical Co) and estrone (99.5 %, Riedel-de Haen Company) were chose as target pollutants.   The P25 photocatalyst (surface area: 50 m^2/g, 80% anatase and 20% rutile, size: 30 nm), was purchased from Germany Company Degussa.   Acetonitrile in analytic grade was purchased from J. T. Baker Co.   All chemicals were used without further treatment and their structures were shown in Table 3-1.
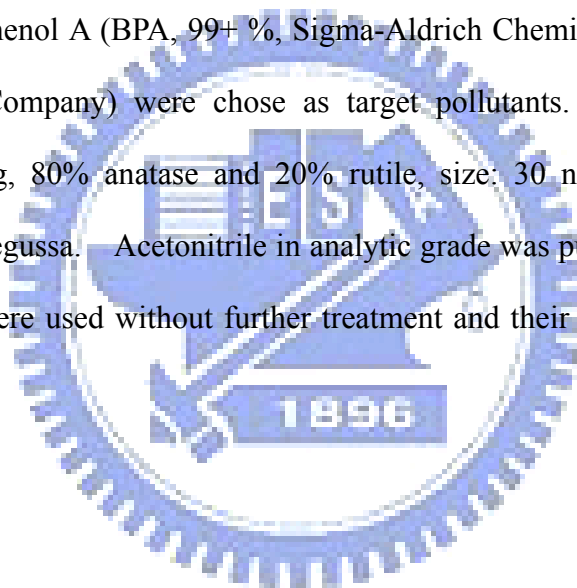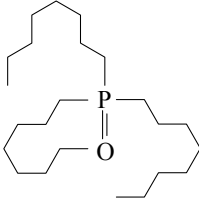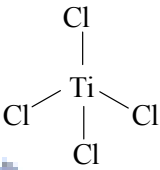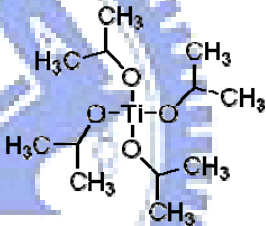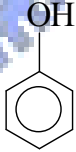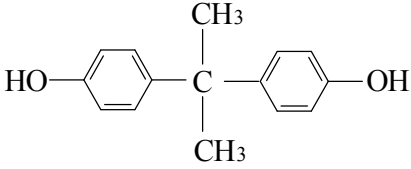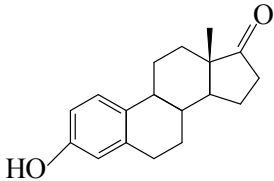
Table 3- 1   The structures of chemicals used in this study.

Chemical	Structure
Trioctylphosphine oxide	
Titanium chloride	
Titanium isopropoxide	
Phenol	
BPA	
Estrone	
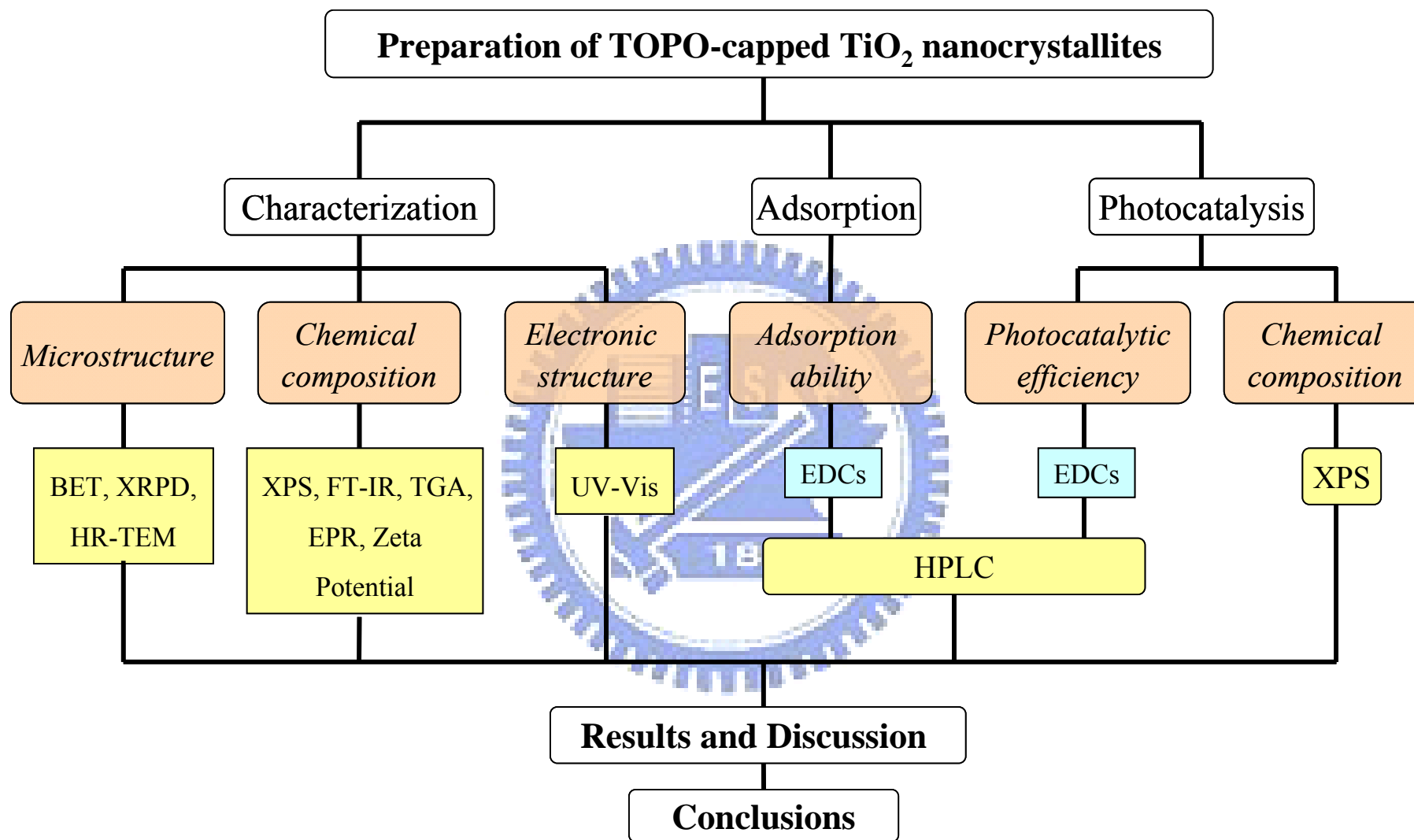
Figure 3- 1   Flow chart of experimental design in this study

3.2   Preparation of TOPO-capped TiO₂ with NHSG method

TOPO-capped TiO_2 are prepared by non-hydrolytic sol-gel process. TOPO (5.22 g, 13.5 mmol) was melted at 80 °C.   By syringe, 0.2744 ml (2.5 mmol) of titanium chloride and 0.7633 ml (2.5 mmol) of $Ti(OC_3H_7)_4$ were injected into the dissolved TOPO.   The suspensions were heated to 150 °C at 500 rpm and kept for 15 minutes.   Following, the well mixed solution was heated to 400 °C under N_2 atmosphere and maintained for 3 hours.   The procedure for preparation of the TiO_2 nanoparticles was illustrated in Figure 3-2.   When the synthesis was completed, the solution became milk-white, then cooled down to 80 °C.   The precipitate TiO_2 nanocrystals were dispersed in acetone, and centrifuged at 11000 rpm for 10 minutes.   This washing step was repeated for three times in order to remove excess TOPO. The resulting sample was dried at room temperature and then grinded with agate mortar into fine powders.   A flow diagram for preparation of TOPO-capped TiO_2 by using non-hydrolytic sol-gel process is shown in Figure 3-3.
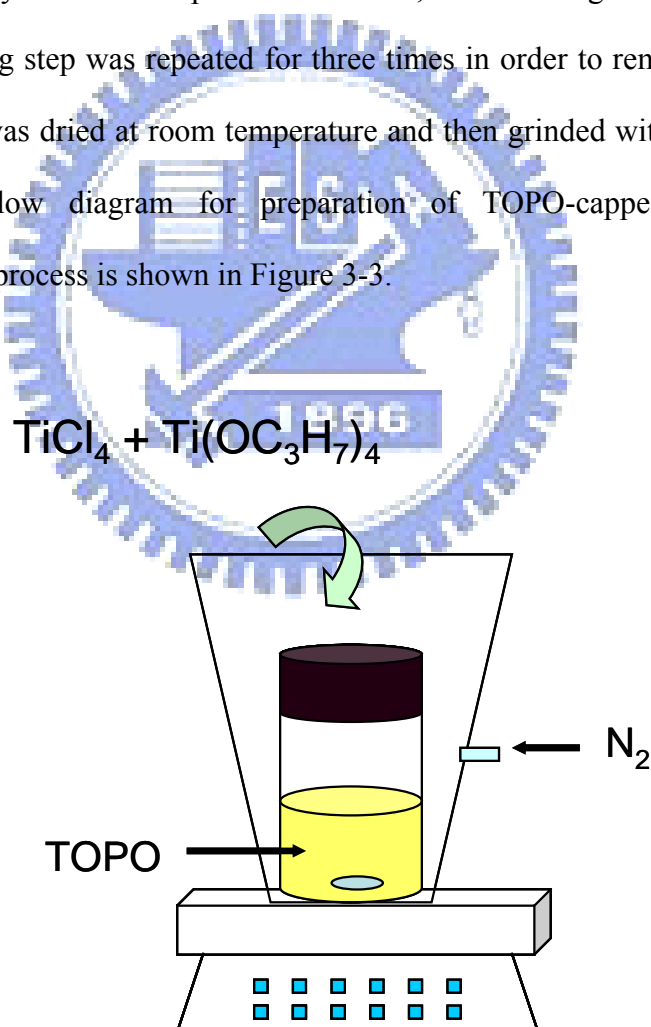
Figure 3- 2   The apparatus for preparation of TOPO-capped TiO₂ with NHSG method.
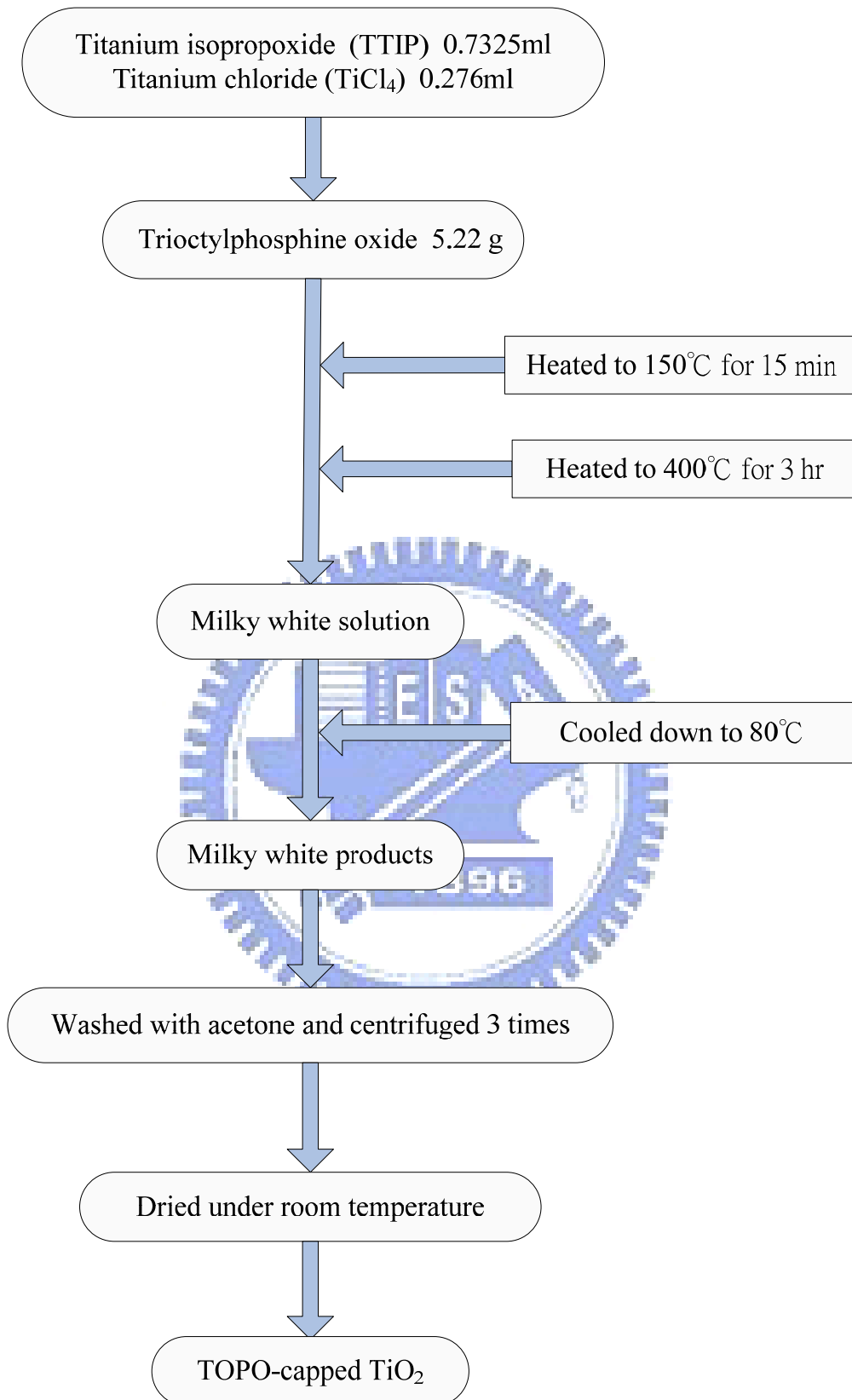
Figure 3- 3   A flow diagram for preparation of TOPO-capped TiO_2 with NHSG method.

3.3   Characterization

3.3.1   X-ray powder Diffractometer (XRPD)

The crystal structure and grain size were examined by X-ray powder Diffractometer (XRPD, Rigaku XRD) using CuKα radiation (λ = 1.5405 Å).   The operating conditions are at an emission voltage of 30 kV and an emission current of 20 mA.   XRPD patterns were obtained between 20° and 90° 2θ range at sample width of 0.02° with scan speed of 4° /min.   The diameter of the crystal was estimated using Scherrer's equation[81]

$$D = \frac{K\lambda}{\beta \cos\theta}$$

D: crystalline size

K: shape constant, 0.89

λ: wavelength of X-ray source (Cu kα = 0.15406 nm)

β: full width at half-maximum (FWHM)

θ: scattering angle

3.3.2   High Resolution Transmission Electron Microscopy (HR-TEM)

The morphology and particle size of the NHSG-derived TiO_2 were identified using high resolution transmission electron microscopy (HR-TEM, JEOL JEM-2010) operated at a 200 kV accelerating voltage.   Suitable transmission specimens were prepared by ultrasonic vibration to disperse TOPO-capped TiO_2 in acetone.   And a drop of the suspension was directly on TEM Cu grids.

3.3.3   X-ray photoelectron Spectroscopy (XPS)

The surface chemical compositions and chemical state of the TOPO-capped TiO_2 were

characterized by X-ray photoelectron spectroscopy (XPS, Physical Electronics, ESCA PHI 1600) using an Al Kα X-ray source (1486.6 eV). The pressure in the analysis chamber was maintained less than 1.4×10^{-9} Torr during all analytical process. The photoelectron was collected with pass energy of 23.5 eV. The collection step size in wide range scan and high-resolution scan analysis are 1.0 eV and 0.1 eV, respectively. In order to quantify and qualify of each element, the curves were fitted by using XPS fitting programs. After performing a subtraction of the "Shirley-shaped" background, the original spectra were fitted using a nonlinear least-square fitting program and combination of Lorentzian and Gaussian lines of variable proportions. The binding energy (BE) scales for the TOPO-capped TiO_2 were referenced by setting the O (1s) line at 530.2 eV.

The integrated peak areas of spectra were calculated using sensitivity factors to determine the surface atomic ratios. The atomic ratio equation is in the following manner:

$$\frac{n_1}{n_2} = \frac{I_1/ASF_1}{I_2/ASF_2} = \frac{A_1/ASF_1}{A_2/ASF_2}$$

n: atomic number

I: intensity of XPS spectra

ASF: atomic sensitivity factor

A: peak area of XPS spectra

3.3.4 Specific Surface Area

The specific surface area of the TiO_2 nanocrystals was calculated from Brunauer-Emmett-Teller model based on the N_2 adsorption and desorption isotherm at 77 K by Micromeritics, ASAP 2020. Prior to N_2 adsorption, the sample was pre-dried at 90 °C for 3 hours in the oven and degassed at 120 °C under vacuum for 90 minutes.

3.3.5 Fourier Transform Infrared Spectrometer (FTIR)

The surface functional groups of the TOPO-capped TiO_2 nanoparticles were recorded with Fourier Transform Infrared spectrometer (FTIR, HORIBA FT-720) scanning from 400-4000 cm^{-1}. All spectra were collected at a resolution 4 cm^{-1} for 100 scans. Samples for FTIR measurement were mixed with KBr (sample: KBr = 1:99, weight ratio) and pressed as a wafer. Further, the spectrum of KBr is the background.

3.3.6 UV-vis Spectrometer

The wavelength response range of the TiO_2 was estimated using UV-vis spectrometer (HITACHI U-3010) using Al_2O_3 as reference. Absorption spectroscopy was carried out in the wavelength region of 200-800nm. The band gap of the TiO_2 was determined from the onset of the absorption spectra which were obtained by conversion of the reflectance spectra using Kubelka-Munk equation.[82]
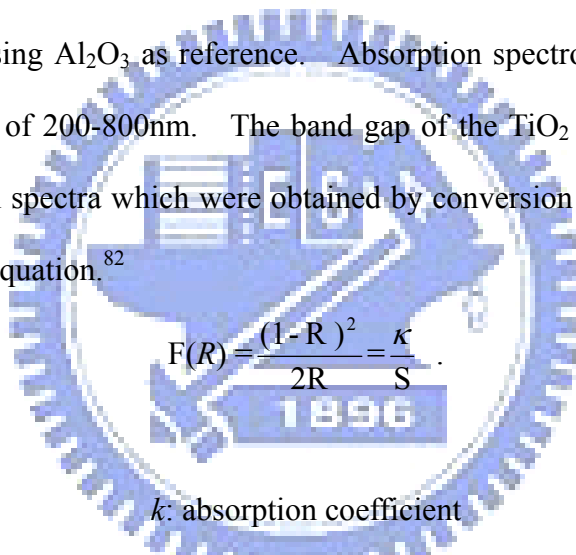
$$F(R) = \frac{(1-R)^2}{2R} = \frac{\kappa}{S}$$.

k: absorption coefficient

S: scattering coefficient

R: %R reflectance

3.3.7 Thermo gravimetric Analysis (TGA)

Thermo gravimetric analysis (TGA) of the nanoparticles was carried out on a TG 209 F1, NETZSCH, Germany. Samples placed in alumina crucibles were heated from 20 °C to a maximum temperature of 900 °C at a heating rate of 10 °C/min under 20 ml/min air flow rate. TGA provided information on weight variation during temperature increase. A weight loss of the sample results from the oxidation of sample to form volatile compounds.

3.3.8 Dynamic Light Scattering (DLS) and Zeta Potential

The hydrodynamic diameter was measured by Zetasizer nano series (Malven Company). In this measurement, sample preparation based on the experiment parameter. The solution containing photocatalysts (1mg/1ml) and target EDCs well mixed by ultrasonic vibration. The concentrations of phenol and BPA were 20 ppm, and that of estrone was 5ppm, whose have been used in this experiment.

The zeta potential of EDCs solution contained nanoparticles was measured by Zetasizer nano series (Malven Company). The concentration of catalysts in the solution was 1mg/1ml. In order to obtain the surface zero point charge of nanoparticles, we use NaOH (3 N) and HCl (3 N) to adjust the pH value of solution.

3.3.9 Electron Paramagnetic Resonance (EPR)

EPR spectra were recorded at the X-band with a Bruker EMX-10/12 spectrometer. The spectrum was recorded using following parameters: 5.02×10^5 receiver gain, 2 G modulation amplitude, 3400-3510 G center field, 200 G sweep width, 9.2-9.8 GHz microwave frequency, and 50.0 modulation frequency. The difference of microwave frequency was related to the catachrestic nature of cylindrical quartz EPR tube. Each catalyst powder was placed in a cylindrical quartz EPR tube with 0.1 g of photocatalysts. Computer simulations were used when necessary to check spectral parameter. The catalyst suspension containing 1g/l or 10 g/l TiO_2 and diluted water were filled in the quartz capillaries with 0.2 ml. To quantify the concentration of hydroxyl radicals generated, signals of radicals spin-trapped with 5,5-dimethyl-1-pyrroline N-oxide (DMPO, Aldrich) were recorded EPR measurement. The 1 ml of 0.03 M DMPO solution was added into 10 ml TiO_2 suspension. Photoirradiation of the samples were carried out with a 500 W Xe lamp (Ushio Inc.) with central wavelength at 365 nm. EPR samples were analyzed at room temperature or 77 K.

3.4 Partition ability of EDCs

An aqueous suspension of EDCs (phenol, BPA and estrone) and TiO_2 was contained in a Pyrex glass vessel and was stirred for 30 minutes in the dark to permit the partition equilibrium to be reached. A 3 ml aliquot was taken at various intervals and centrifuged at 15000 rpm for 3 minutes immediately for separation of the suspended solids. Then, the supernatants were analyzed by HPLC measurement. In the partition isotherm experiments, the initial concentrations were adjusted to various concentrations (20-100 ppm for phenol and BPA and 1-5 ppm for estrone) and mixed with photocatalysts. Partition behaviors were obtained by mixing EDCs and 1mg/ml of TiO_2 amounts and stirred 30 minutes. EDCs solutions with initial concentrations ranging from 10 to 100 ppm were used to get the partition behaviors.

3.5 Photodegradation of EDCs

The experimental apparatus for the photodegradation of EDCs was shown in Figure 3-4. A quartz water-jacketed reactor was carried out under illumination of UV light at 305 nm. For safety reason, the reactor was completely surrounded by stainless steel. The solutions containing photocatalysts (1mg/ml) and target phenol, BPA or estrone were well mixed using ultrasonic bath. The photocatalytic decompositions of EDCs were investigated at room temperature by varying the initial concentration from 2.5 to 50 ppm. Before illumination, the suspensions were purged with oxygen and magnetically stirred in the dark for 30 min. The degradation efficiency was examined by analyzing the changes in the concentration of the EDCs at each time interval during photocatalysis. These samples were periodically sampled by withdrawing aliquots from the photoreactor; it was centrifuged at 15000 rpm for 3 minutes prior to analysis. These clean solutions were monitored by HPLC measurement.

Figure 3- 4　　Photoreactor and the wavelength of UV-lamp is 305 nm in our study.

3.6　High Performance Liquid Chromatography (HPLC)

The concentration of EDCs (phenol, BPA and estrone) was analyzed by High Performance Liquid Chromatography (HPLC, Waters Alliance 2695) equipped with a Photodiode Array Detector (PDA, Waters 2996, 190-400 nm) at room temperature. The stationary phase is C18 (5μm, 4.6×250 mm) for phenol and BPA and dC18 (3μm, 2.1×20mm) column for estrone. The mobile phases for the phenol and BPA were methanol-water mixture (50/50, v/v) and acetonitrile–water mixture (50/50, v/v), respectively, at flow rate of 1.0 ml/min. Signals were detected at 280 nm. Methanol-water mixture at 50/50 volume ratio and flow rate of 0.6 ml/min with dC18 column was used for estrone analysis. Signals were detected at 195 nm. Figure 3-5 shows flow diagram of photocatalysis of EDCs in this study.
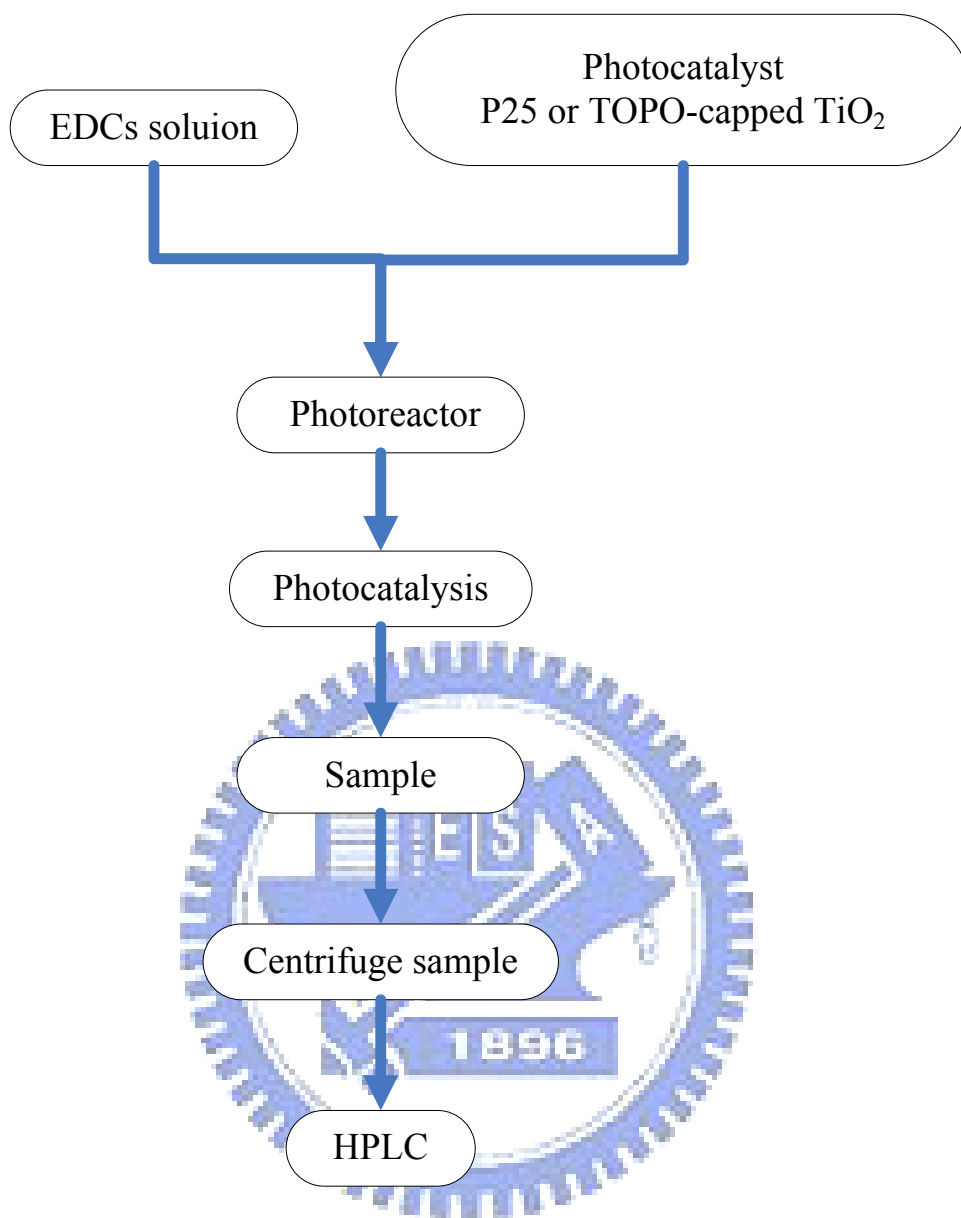
Figure 3- 5   A flow diagram for photocatalysis of EDCs.

Chapter 4.   Results and discussion

4.1   Physicochemical properties of TOPO-capped TiO$_2$

4.1.1   Microstructures of TOPO-capped TiO$_2$

The surface composition was examined using XPS.   In addition to Ti(2p) and O(1s), P(2p) photoelectron peaks were also found in the XPS spectra (Figure 4-1), indicating the existence of TOPO on the TiO$_2$ surface.   FT-IR spectra of TOPO-capped TiO$_2$ sample in the 900-1260 cm^{-1} region is shown in Figure 4-2.   The pure TOPO molecules is characterized by P=O vibration frequency appearing strongly at 1148 cm^{-1}.   In the spectrum of the non-hydrolytic sol-gel-derived TiO$_2$, there appeared a lower vibration frequency at 1085 cm^{-1}. It can be regarded that the TOPO is chelated to the TiO$_2$ surface as P=O→Ti during NHSG process at high temperature.   The shift of the P=O absorption toward higher energy after modification is due to the strong interaction existing at the interface of TOPO and TiO$_2$.
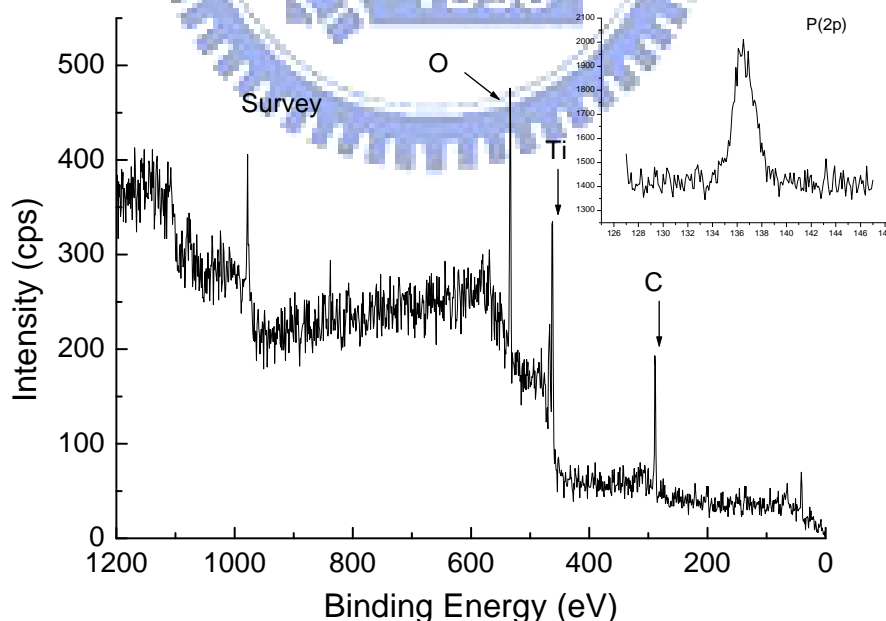
Figure 4- 1   XPS spectra of TOPO-capped TiO$_2$.
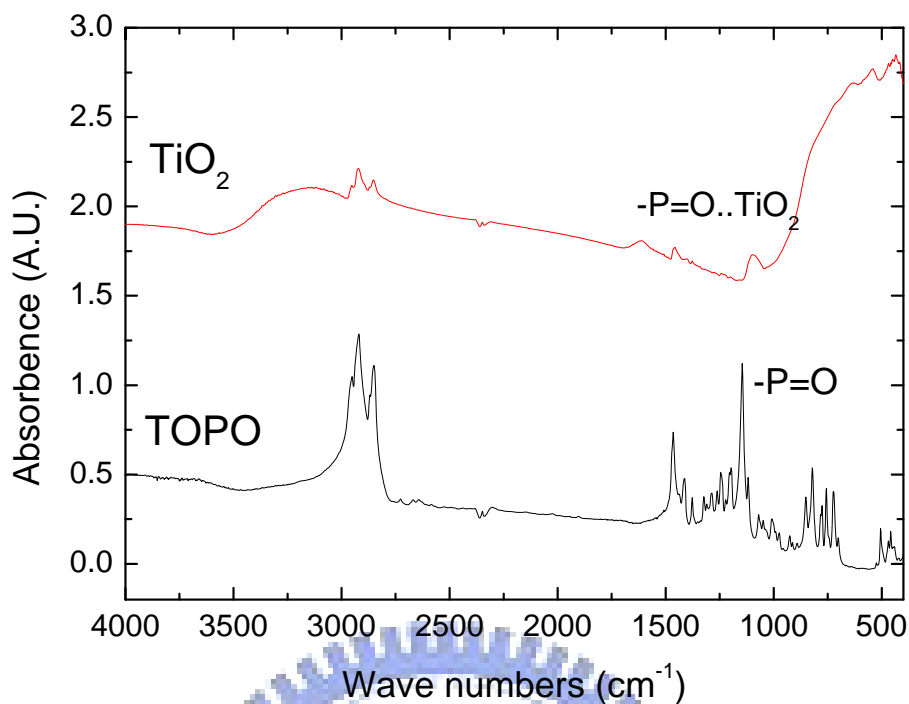
Figure 4- 2　FTIR spectra of TOPO and TOPO-capped TiO_2.

Thermo gravimetric analysis (TGA) was applied to estimate the quantity of TOPO on the TiO_2 surface.　Figure 4-3 shows the TGA profile of TOPO-capped TiO_2 sample.　A total weight loss of TOPO-capped TiO_2 was 20.1 % from ambient temperature to 550 °C which can be divided into two steps.　The 4.01 % weight loss of the TOPO-capped TiO_2 bellow 150 °C corresponds to removal of water.　In the second step of weight loss suggests to the surface TOPO compound was completely decomposed at 550 °C.　Moreover, 16.09 % of TOPO molecules are on the TiO_2 surface.
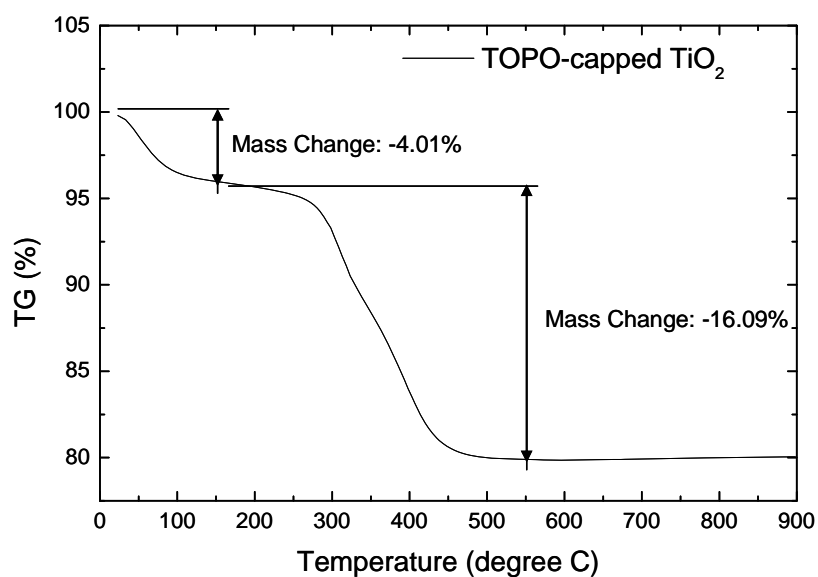
Figure 4- 3   The TGA curve of TOPO-capped TiO$_2$.

The crystalline properties of TOPO-capped TiO$_2$ were determined by XRD (See Figure 4-4). The diffraction peak of (101) profile at 25.4° 2θ indicates that the TiO$_2$ sample is mainly anatase form. From the broadness of the diffraction peak of TOPO-capped TiO$_2$, the average crystallite size calculated by Scherrer's equation is 4.9 nm. The high resolution transmission electron micrograph, shown in Figure 4-5, indicates that TOPO-capped TiO$_2$ sample have negligible agglomeration. TOPO-capped TiO$_2$ sample were well crystallized even for grains as small as 5 nm. There is no doubt that synthesis of metal oxide by non-hydrolytic sol-gel process can prepare homogeneous nanoparticles with well crystalline phase.[37-40] Further, TOPO acts as capping agent to the TiO$_2$ particles, leading to maintain the nanoscale size and have well crystallinity.[27] The specific surface area of the TOPO-capped TiO$_2$ determined by BET method was 7 m^2/g. This value is far less than its theoretical one (488 m^2/g). The difference between the experimental and theoretical results is mainly resulted from the TOPO which contributes 16 % to total mass of sample and leads to aggregation of nanocrystals in dry.
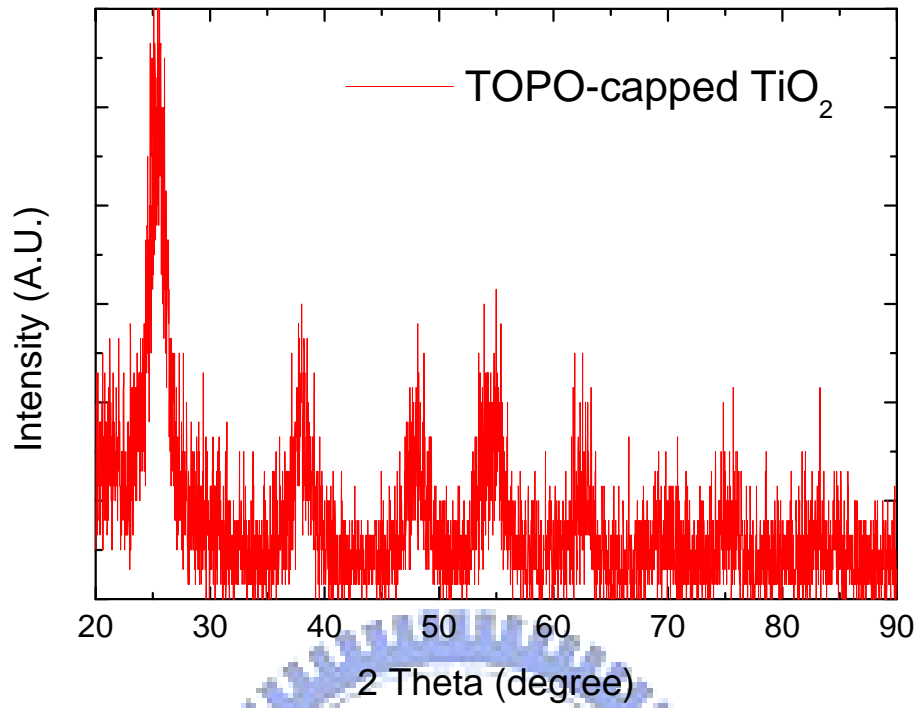
Figure 4- 4   The XRD pattern of TOPO-capped TiO$_2$.
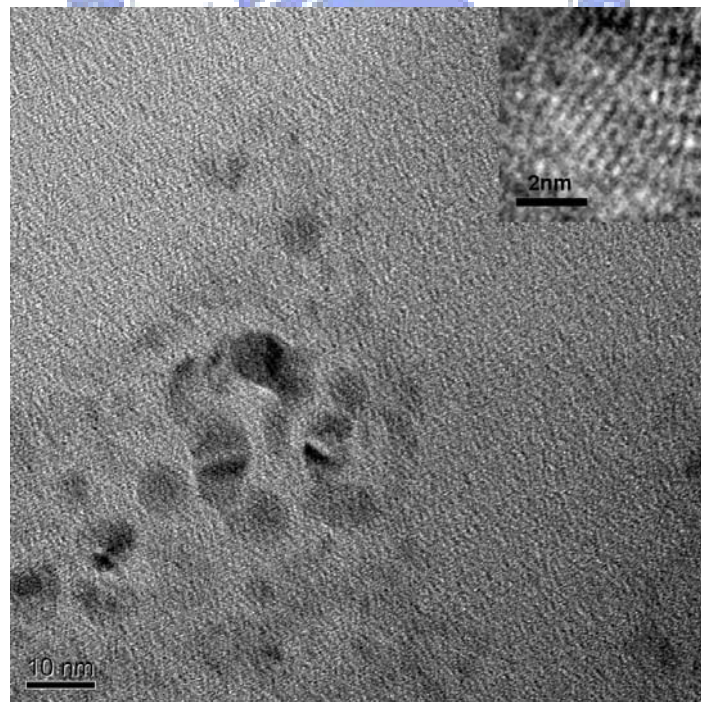
Figure 4- 5   HRTEM image of TOPO-capped TiO$_2$.

Semiconductor can be produced photoinduced electrons and holes when the excited energy is greater or equal to the bandgap energy. The optical property of TOPO-capped TiO_2 was examined by UV-Visible spectrum. Figure 4-6 shows the UV-Vis absorption spectrum of TOPO-capped TiO_2. A steep absorption was measured below 350 nm. A bandgap of 3.54 eV of the TOPO-capped TiO_2 was obtained from the absorption edge. According to the quantum size effect (10-100 Å), the band gap energy is blue-shifted toward the decreased particle size.[32] The band gap of the TiO_2 nanocrystals in this study is larger than their bulk one (3.2 eV), indicating the quantum size scale of the non-hydrolytic sol-gel derived nanocrystals.
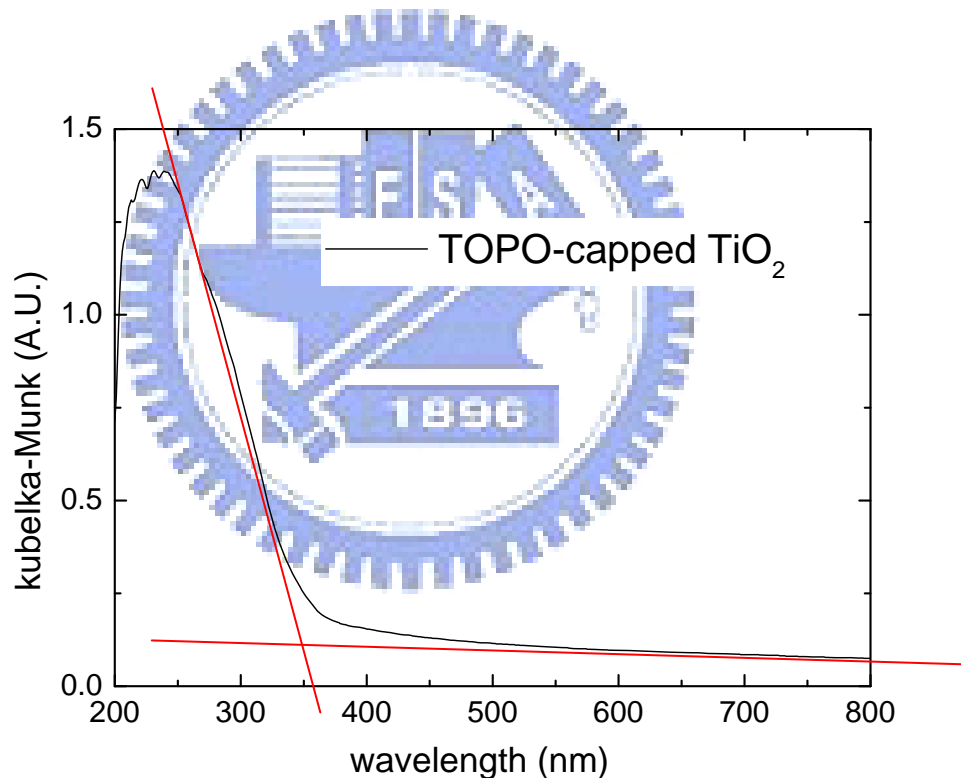
Figure 4- 6   UV-Vis absorption spectrum of TOPO-capped TiO_2.

4.1.2   Isoelectric point and Hydrodynamic diameter of TiO_2

The affinity interaction between the catalyst TiO_2 and reactants is considered to enhance the catalytic reaction rate. The diffuse of organic compounds in the liquid phase to the TiO_2 surface due to the catalyst surface charge. The pH value of aqueous solution significantly

influences the surface charge of the semiconductor particles and the charge forms of the compounds.   When the zeta potential of the particle closes to zero, this condition is called isoelectric point (IEP).   According to the following equations, TiO_2 surface is negatively charged at the pH value higher than the IEP of TiO_2 (Eqn. (4-1)), whereas positively charged at pH< IEP (Eqn. (4-2)).

$$pH \; > \; IEP : Ti\text{-}OH + OH^- \rightarrow TiO^- + H_2O \qquad (4\text{-}1)$$

$$pH \; < \; IEP : Ti\text{-}OH + H^+ \rightarrow TiOH_2^+ \qquad (4\text{-}2)$$
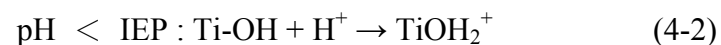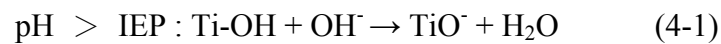
The pH dependent zeta potential of TiO_2 suspensions is shown in Figure 4-7.   The IEP for TOPO-capped TiO_2 in the pure water, phenol or BPA solutions were located at pH 6.2, which was equal to that for Degussa P25.[83]

Figure 4-8 shows the zeta potential of TOPO-capped TiO_2 after photodegradation of phenol or BPA.   The zeta potential maintained around 40 eV even after 4 hours reaction. The surface quantities ratio of oxygen and titanium atoms was 1.2 which is smaller than the stoichiometric value of 2.   Thus, there are substantial amounts of oxygen vacancies on the TiO_2 surface due to the NHSG method.   The dissociation of hydroxyl (OH^-) occupied the sites of oxygen vacancy, and the proton (H^+) caused the acidic phenomenon.   Thus, the mixed solution in the presence of the TOPO-capped TiO_2 became acidic and the zeta potential was 40 eV.   Then, the surface charge of TOPO-capped TiO_2 maintained the 40 eV after photocatalysis, indicating that the characteristic nature of surface properties was changed insignificantly during the photocatalysis.
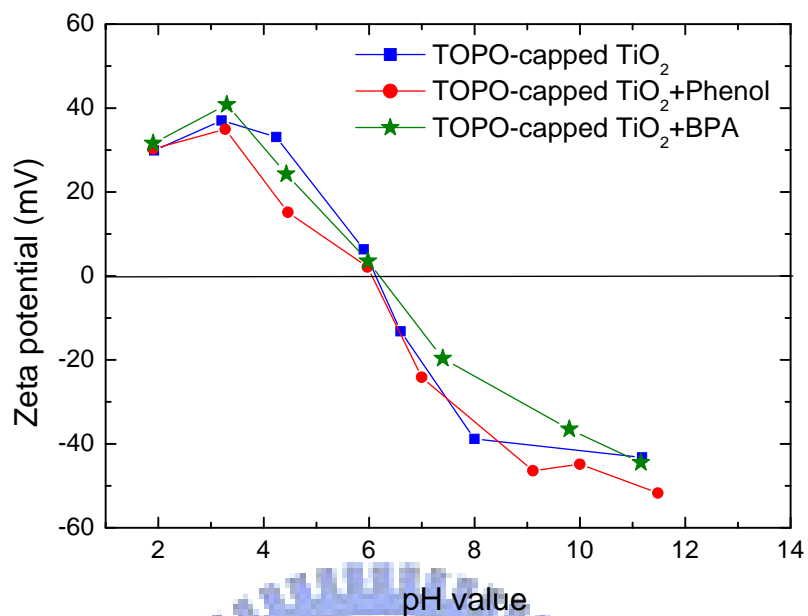
Figure 4- 7   Zeta potential of TOPO-capped TiO$_2$ and mix with phenol and BPA solution.
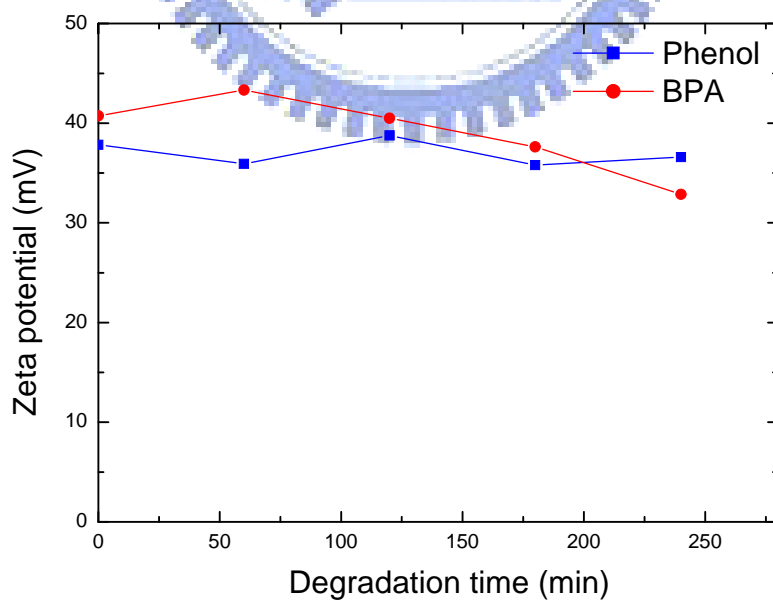
Figure 4- 8   Zeta potentials after photodegradation of phenol or BPA by TOPO-capped TiO$_2$.

In order to elucidate the hydrodynamic diameters of TOPO-capped TiO_2 after EDCs partition, dynamic light scattering was used to analyze the particle sizes of TOPO-capped TiO_2. Table 4-1 tabulated the particle size distribution of TOPO-capped TiO_2 in different kinds of EDCs solutions. The hydrodynamic diameter of the pure TOPO-capped TiO_2 in the DI water was 182.04 nm. The hydrodynamic diameters of TOPO-capped TiO_2 in phenol, BPA and estrone solutions were 215.38, 221.26 and 216.84 nm, respectively. The hydrodynamic diameter of the P25 was 213.97 nm in DI water, and was 278.33, 266.33 and 272.90 nm in phenol, BPA and estrone solutions, respectively. The hydrodynamic diameters of TOPO-capped TiO_2 or P25 in the aqueous solutions are all much larger than their individual particle sizes (5 nm of the TOPO-capped TiO_2 and 30 nm of P25). These phenomena mean that the agglomeration of photocatalyst in the EDCs solution is shown in this experiment containing TiO_2 catalyst. Moreover, the EDCs adsorb on or close to the TiO_2 surface and enlarge the hydrodynamic diameters.

Table 4- 1   Particle size distribution of TOPO-capped TiO_2 in EDCs solution.

Photocatalyst (hydrodynamic diameter, nm)	EDCs	Hydrodynamic diameter (nm)
TOPO-capped TiO_2 (182.04 nm)	Phenol	215.38
	BPA	221.26
	Estrone	216.84
P25 (213.97 nm)	Phenol	278.33
	BPA	266.33
	Estrone	272.90

4.2 Partition Study

4.2.1 Partition equilibrium

Figure 4-9 and 4-10 show the time domain of partition equilibriums for phenol, BPA and estrone on TOPO-capped TiO_2 and Degussa P25 particles, respectively. In the TOPO-capped TiO_2 system, the distributed plateau takes place after 1 min, indicating partition equilibrium of EDCs. The initial concentration of phenol, BPA and estrone were 10 to 50 and 1 to 5 ppm, and the distributed quantities were 2.2 to 4.2, 13 to 50 and 0.9 to 4.4 mg/g, respectively. On the contrary, the adsorbed quantities for phenol, BPA and estrone were closed to 0.2 mg/g because of the affinity of P25 and EDCs were undesired. These finding reveal that the organic molecules were easily distributed to modified TiO_2 surface. The modification leads to the hydrophobic property, thus enhancing the affinity for the hydrophobic EDCs.
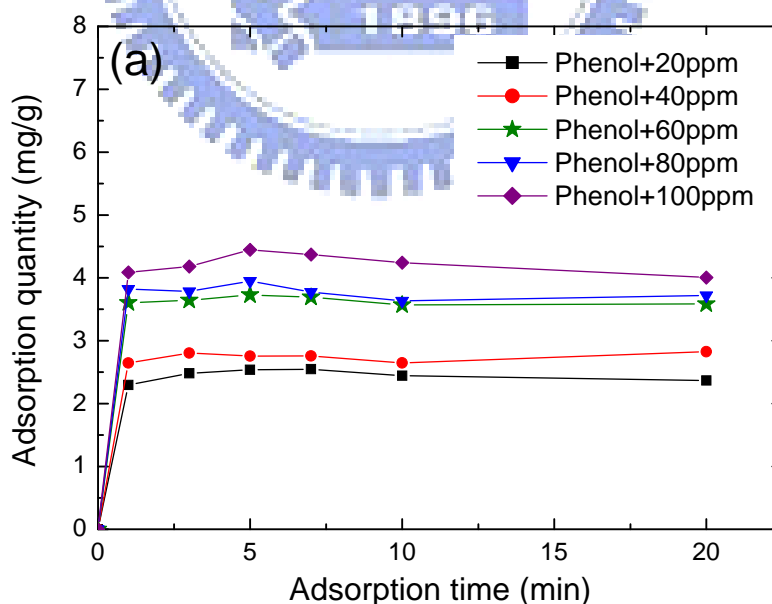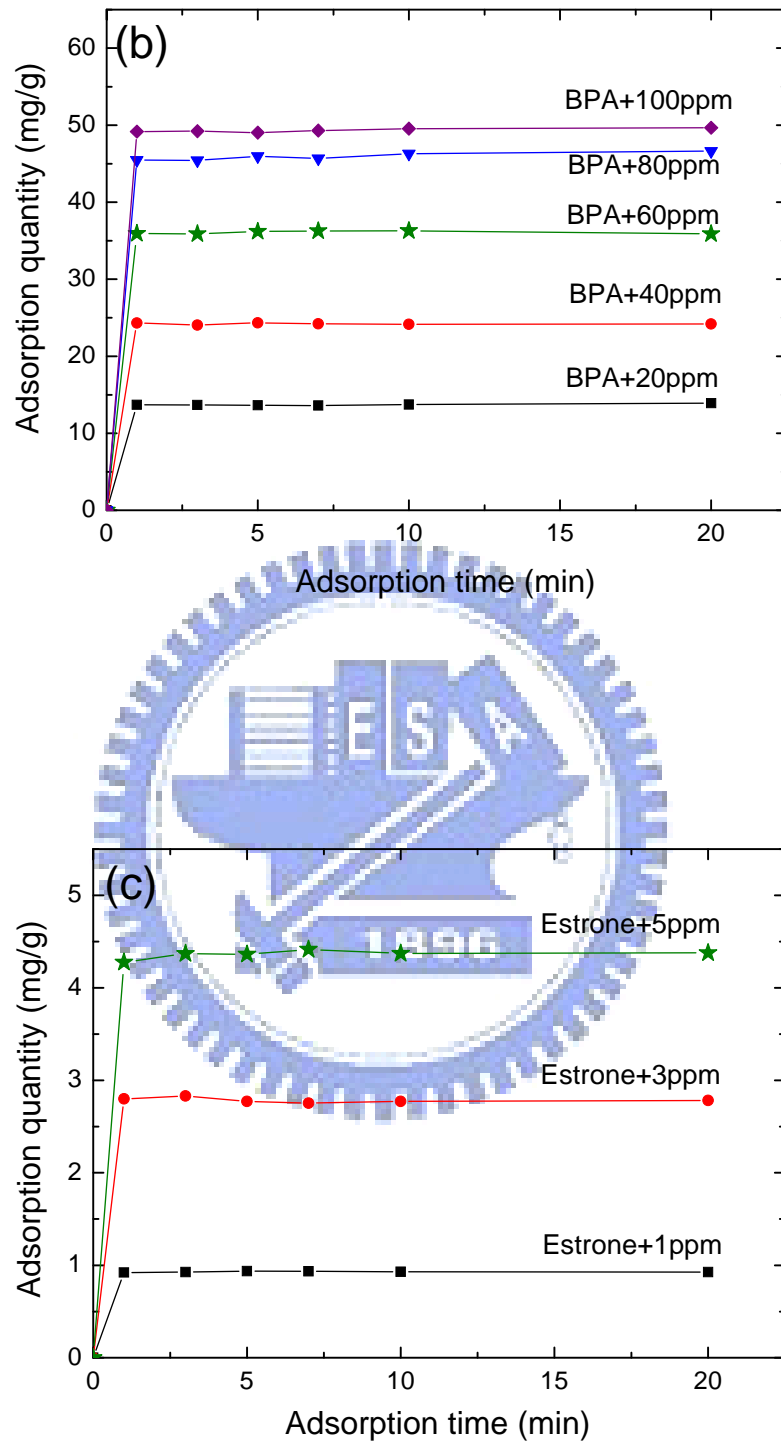
Figure 4- 9   Partition equilibriums for (a) phenol, (b) BPA and (c) estrone on TOPO-capped

TiO$_2$ at 25 °C.
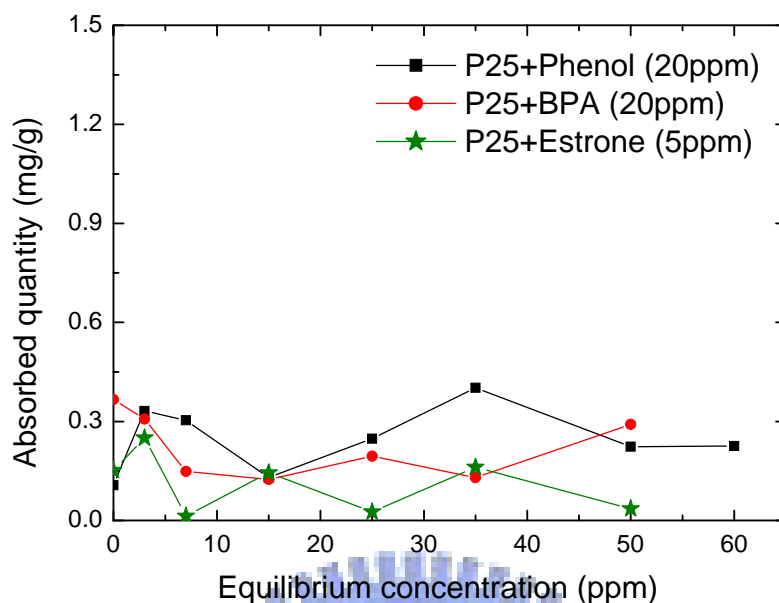
Figure 4- 10   Partition equilibriums for phenol (20 ppm), BPA (20 ppm) and estrone (5 ppm) on Degussa P25.

4.2.2   Partition isotherm

The surface coverage of organic pollutants on the TiO_2 plays a crucial part in the photocatalytic reaction.   Therefore, it is necessary to explicitly determine the distributed behavior of the photocatalysts for the EDCs.   Figure 4-11 shows the partition isotherms for phenol, BPA and estrone in the presence of TOPO-capped TiO_2.   It shows that the distributed quantity of phenol partition maintains in 3 to 4 ppm with increasing concentration. When the equilibrium concentration of BPA is 4 to 21 ppm, the distributed behavior shows 15 to 38 mg/g ability.   Saturated partition of 50 mg/g was observed above 32 ppm.   Estrone can be easily distributed to the TOPO-capped TiO_2 via hydrophobic character.   Figure 4-12 shows the partition isotherms for phenol, BPA and estrone in the presence of Degussa P25. In contrast to the high distributed ability of EDCs on the TOPO-capped TiO_2, the partitions of P25 for phenol, BPA and estrone were insignificant.   This result suggests that the

hydrophobic property leads to the better affinity between TOPO-capped TiO_2 and EDCs.   In the case of TOPO-capped TiO_2, the distributed quantities increase with increasing the concentrations of EDCs and attain to saturation.
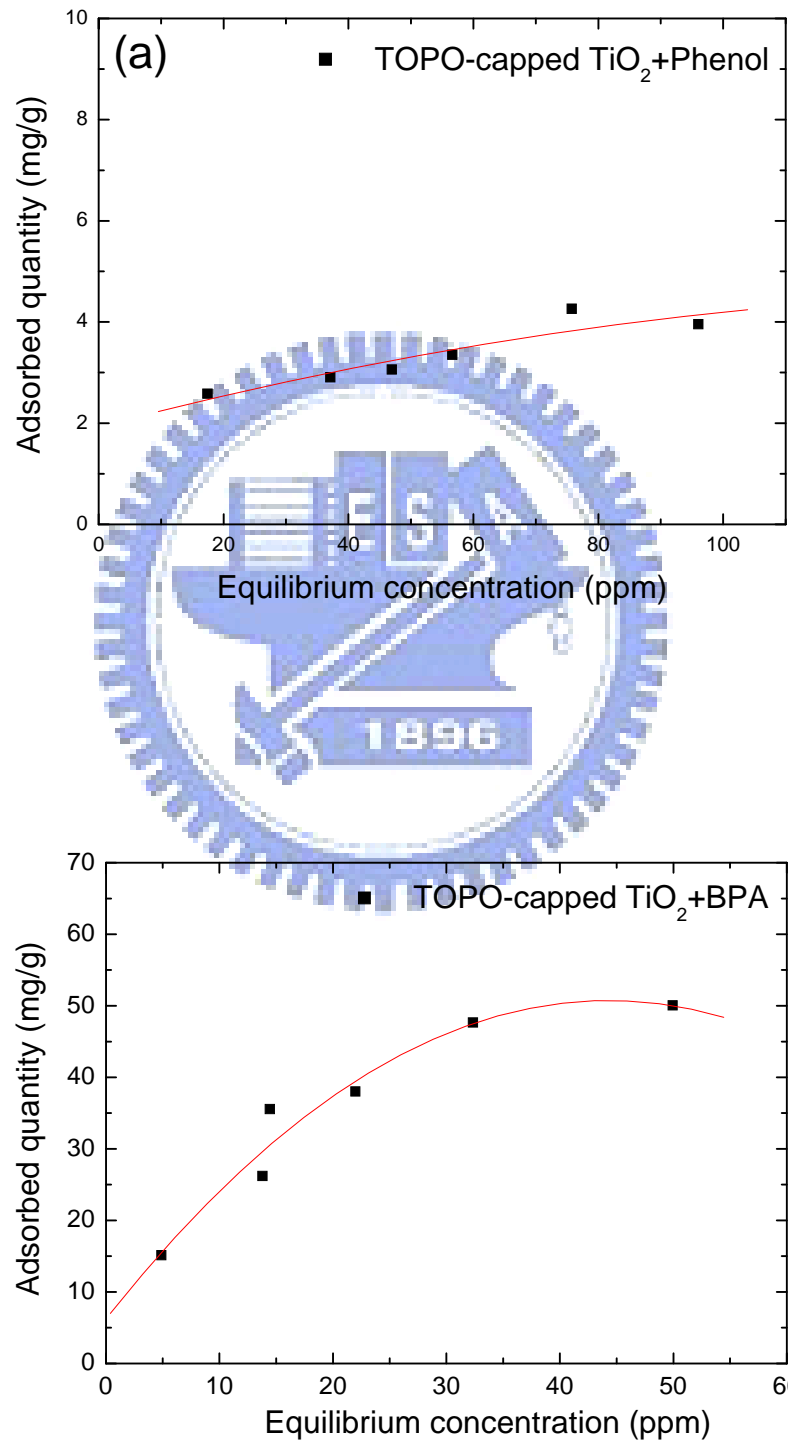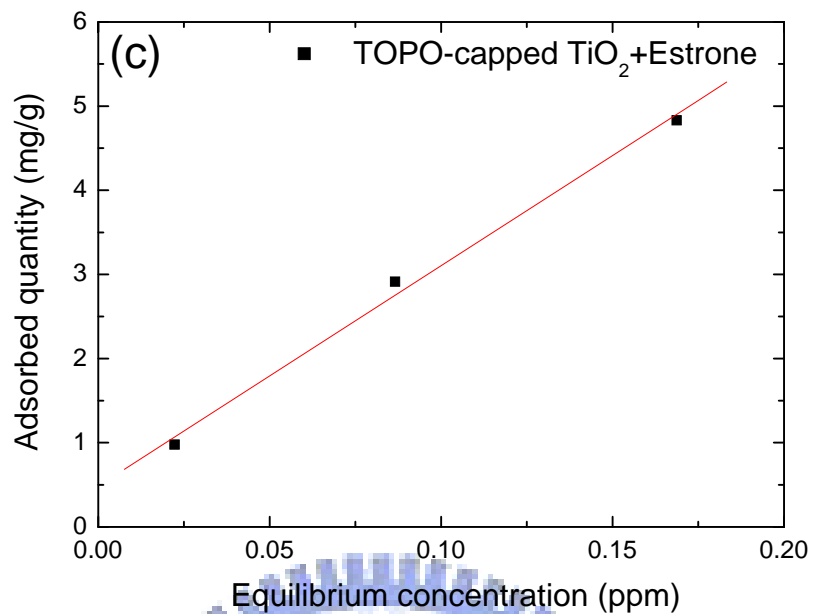
Figure 4- 11   Partition activity for (a) phenol, (b) BPA and (c) estrone in the presence of
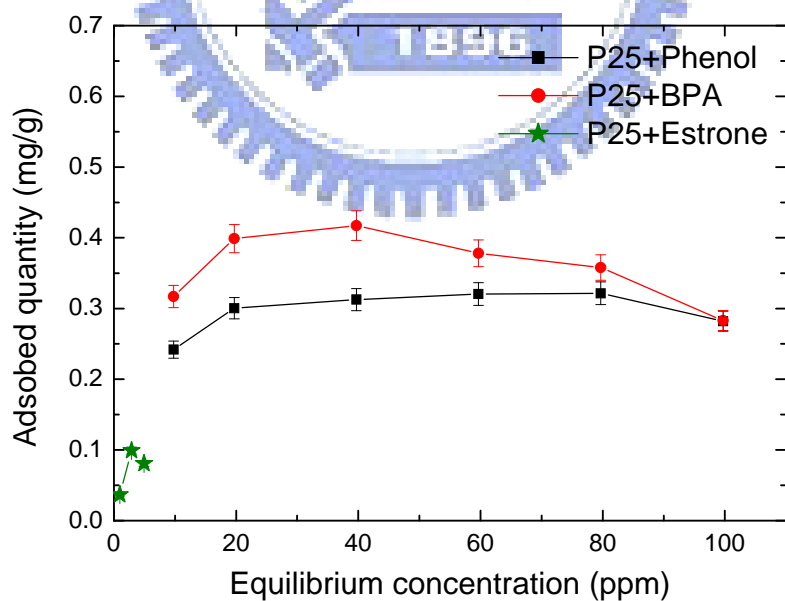
TOPO-capped TiO$_2$.

Figure 4- 12   Partition activity for phenol (a), BPA (b) and estrone (c) in the presence of

Degussa P25.

In this study, partition is nonspecific adsorption, which ascribes the affinity between EDCs and TOPO-capped TiO_2. This equilibrium constant K is defined as distribution of EDCs between the TOPO-capped TiO_2 and water. For the solute species A, the relationship has been written

$$A_{water} \Leftrightarrow A_{TOPO\text{-}capped\ TiO2}$$

The description of the equilibrium constant K used in this reaction is partition coefficient, and is defined as

$$K = \frac{C_{TOPO-cappedTiO2}}{C_{water}}$$

Where $C_{TOPO\text{-}capped\ TiO2}$ is the concentration of the solute on the surface of TOPO-capped TiO_2 (mg/g) and C_{water} is its concentration in the water (ppm).

The partition coefficients in this study were obtained from the partition equilibrium experiment. The values of partition coefficient were calculated by the concentration of EDCs in the aqueous solution to that in the solid phase, which can be described the degree of the distributed abilities of EDCs in the presence of TiO_2. The log K_{ow} values and partition coefficients K are summarized in Table 4-2. The partition coefficients of TOPO-capped TiO_2 for phenol, BPA and estrone were 0.15, 3.09 and 28.64 (l/g), respectively. The partition coefficients of P25 for phenol, BPA and estrone were 1.5×10^{-2}, 2.0×10^{-2} and 1.6×10^{-2} (l/g), respectively. These results clearly show the ranks of partition coefficients are TOPO-capped TiO_2 > P25 in the EDCs solutions. Moreover, the distributed abilities in the presence of TOPO-capped TiO_2 were ranked as estrone > BPA > phenol, which are similar to the trend of their log K_{ow}. This is because of the EDCs can adsorb on organic modified TiO_2 via the hydrophobic property leading to the higher partition coefficients.

Table 4- 2   The log Kow value and partition coefficient for phenol, BPA and estrone with TOPO-capped TiO_2 and P25.

		Phenol	BPA	Estrone
Partition coefficient, K	**TOPO-capped TiO_2**	0.15	3.09	28.64
	P25	1.5×10^{-2}	2.0×10^{-2}	1.6×10^{-2}
log K_{ow}		1.46	2.2	3.13

4.3   EPR spin trapping of hydroxyl radicals for TiO_2 powders

Semiconductors, TiO_2, were illuminated by enough energy to separate the electrons and holes.   Then photogenerated carriers trapped at the TiO_2 surface and reacted with surface adsorbed molecules to produce free radical species with very short lifetime.   Electron paramagnetic resonance (EPR) has been used frequently due to its sensitivity and the ability to determine the information on its structure and location.   All the signals in the EPR spectra were described by the sets of g values.[84, 85]

Figure 4-13 shows the EPR spectra of the radicals formed upon irradiation of UV and/or microwave of photocatalysts at room temperature.   These four samples characterized by the set of g values, g_1=2.012, g_2=2.01, g_3=2.004 and $g_{//}$=1.964, $g_\perp$=1.981.   The TOPO-capped TiO_2 exhibited that photogenerated holes trapped on or near the particle surface to form Ti^{4+}-O^--Ti^{4+}-OH^- radicals.   In addition, the electrons were trapped at the TiO_2 surface to form surface Ti^{3+}. Another broad signal appeared at g_1=2.024, g_2=2.009, g_3=2.003, which is assigned the Ti^{4+}-O_2^- on anatase.[84, 85]   After integration of the EPR spectra, the intensities among different photocatalyst and experiment conditions were compared.   TOPO were modified on TiO_2 surface, therefore, the EPR intensity need to normalize the real quantity of

TiO$_2$ contained in the sample (per gram of TiO$_2$). Table 4-3 shows the intensities of Ti^{4+}-O$^-$-Ti^{4+}-OH$^-$ radical of TOPO-capped TiO$_2$ and P25 TiO$_2$ by integrations of EPR spectrum. The intensity of Ti^{4+}-O$^-$-Ti^{4+}-OH$^-$ of TOPO-capped TiO$_2$ is 1.78 times higher than that of P25 under UV illumination at room temperature. These results reveal that TOPO-capped TiO$_2$ can inhibit the charge recombination and accelerate the radicals producing. The crystal size of TOPO-capped TiO$_2$ and P25 are 5 and 30 nm, respectively. The photogenerated holes can migrate to the TiO$_2$ surface quickly and produce free radicals in the smaller particle size of TOPO-capped TiO$_2$.

Figure 4-14 shows the EPR spectra of the radicals formed upon irradiation of UV and/or microwave of photocatalyst at 77K. Under UV illumination at 77K, photogenerated electrons were tapped in the inner part of Ti^{3+} species and gave the signal Ti^{3+}. The signals at g$_1$=1.961, g$_2$=1.992, g$_3$=1.992 were ascribed to substitutional Ti^{3+} in hydrated anatase. The signals at g$_1$=2.024, g$_2$=2.009, g$_3$=2.003 were formed on anatase after UV irradiation and O$_2$ molecules adsorption, which was assigned the Ti^{4+}-O$_2^-$ on anatase.[84, 85] The intensity of the Ti^{4+}-O$_2^-$ on anatase of TOPO-capped TiO$_2$ is 1.18 times higher than that of P25 under UV illumination at 77K.(Table 4-4) This result shows that the TOPO-capped TiO$_2$ can improved interfacial charge transfer and accelerate the radicals producing, due to the smaller crystalline size. Moreover, the photogenerated Ti^{3+} signals were only detected in the TOPO-capped TiO$_2$ particles under UV illumination at 77K, due to recombination of trapped holes and electrons at higher temperature. Ti^{3+} radicals recombined very fast, so that the signals were obtained only at temperatures well bellow 77K. This peak shows that the defects in TOPO-capped TiO$_2$ trapped photogenerated electrons and holes which can react with adsorbed water to form ·OH radicals.[85]

DMPO spin trapping EPR experiments have been carried out to detect the free radical intermediates generated at the surface of the irradiated TiO$_2$. Figure 4-15 shows the EPR spectra of radicals formed from TiO$_2$ in DMPO solution upon UV irradiation at room

temperature.　The DMPO react with hydroxyl radicals and trap them in the form of DMPO-OH· which characterized by the classical 1:2:2:1 relative peak.[86-88]　Table 4-5 shows the integrated intensities of DMPO-OH· radicals generated by illumination of TOPO-capped TiO$_2$ or P25 TiO$_2$.　This result clearly shows the intensity of TOPO-capped TiO$_2$ increased with increasing the TiO$_2$ content.　When the mass ratio of P25 and water is 1:1, the intensity is much higher than that of TOPO-capped TiO$_2$.　This result is described that P25 can increase the adsorption of oxygen and water due to the hydrophilic and smooth surface character.　The photogenerated charge carriers react with adsorbed molecules easily and directly.　Thus, the intensity of DMPO-OH· of TOPO-capped TiO$_2$ is smaller than that of P25 after illumination.
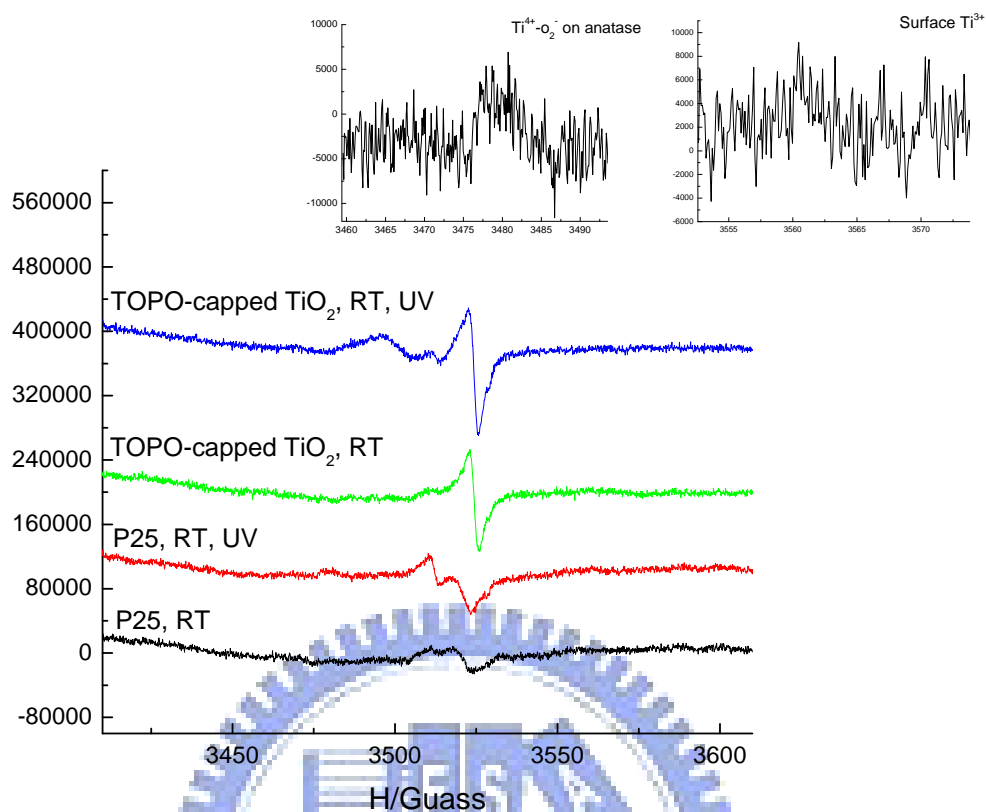
Figure 4- 13   EPR spectra of the radicals formed upon irradiation of UV and/or microwave

of photocatalysts at room temperature.

Table 4- 3   The intensities of Ti^{4+}-O^--Ti^{4+}-OH^- obtained from the integrations of the spectra.

TiO$_2$ powder	Intensity
TOO-capped TiO$_2$ (RT+UV)	1.6×10^6
TOO-capped TiO$_2$ (RT)	1.1×10^6
P25 (RT+UV)	9.0×10^5
P25 (RT)	4.1×10^5
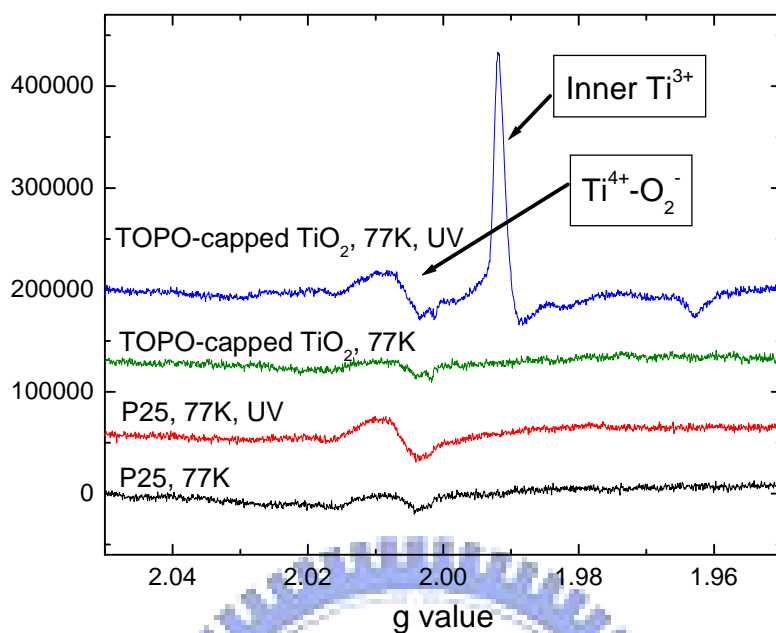
Figure 4- 14   EPR spectra of the radicals formed upon irradiation of UV and/or microwave of photocatalysts at 77K.

Table 4- 4   The intensities of the Ti^{4+}-O_2^- on anatase obtained from the integrations of the spectra.

TiO$_2$ powder	Intensity
TOPO-capped TiO$_2$ (77K+UV)	3.9×0^6
TOPO-capped TiO$_2$ (77K)	1.7×10^6
P25 (77K +UV)	3.3×10^6
P25 (77K)	1.3×10^6
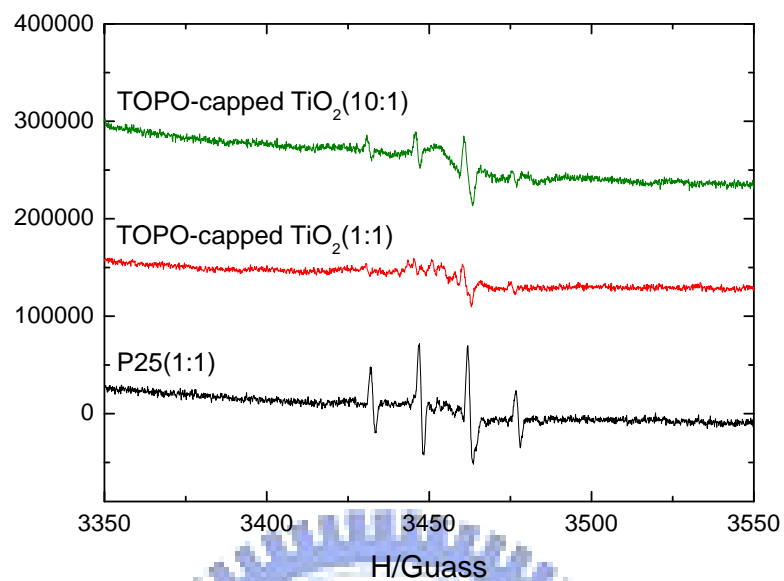
Figure 4- 15   EPR spectra of radicals formed contained hole scavenger, DMPO, upon UV irradiation at room temperature.

Table 4- 5   The intensities of DMPO-OH· obtained from the integrations of the spectra.

Solution contained TiO$_2$ and DMPO	Intensity
TOPO-capped TiO$_2$ (10:1)	3.2×10^5
TOPO-capped TiO$_2$ (1:1)	1.3×10^5
P25 (1:1)	3.8×10^5

4.4 Photocatalysis Study

4.4.1 Photocatalytic activity

In this study, photocatalysis of phenol and BPA had three steps in the presence of TOPO-capped TiO_2. First, the EDCs transferred from mixed solution to the TOPO-capped TiO_2 surface. Then, the adsorbed compounds diffused to the surface of photocatalysts. Finally, the surface reaction took place between the photogenerated charge carriers and radicals and the EDCs on the TiO_2 surface.

The photocatalytic activities of TOPO-capped TiO_2 and Degussa P25 were measured by decomposition of phenol and BPA. Figure 4-16 and 4-17 show the concentration dependent decomposition kinetics of phenol and BPA in the presence of TOPO-capped TiO_2 or P25. When the TiO_2 suspensions were irradiated with UV light, the EDCs concentration decreased obviously with illumination time. After illumination time of 360 min, phenol and BPA were destroyed completely in the photocatalytic reactions. For the photocatalysis of phenol in the presence of TOPO-capped TiO_2, the decomposed reaction delay in the first 10 to 20 minutes. This lag is resulted from weak affinity between this catalyst and phenol. Phenol diffused to the TOPO-capped TiO_2 surface hardly, and the photocatalytic processes were delayed in the beginning. Therefore, after dynamic equilibrium, the surface reaction turned to the dominant rate-limiting step. The initial rates were calculated after 10 to 20 minutes. On the other hand, the BPA can distribute to the surface of TOPO-capped TiO_2 easily, the dominant rate-limiting step in the BPA system was surface reaction. Subsequently, the dominant rate-limiting step of the photocatalysis for phenol and BPA in this study was surface reaction. Thus, these photocatalytic reactions can be described by Langmuir-Hinshelwood kinetics model.

There are several assumptions were established for the Langmuir-Hinshelwood kinetics:

(1) The number of adsorbed sites on the catalyst surface is finite,

(2) The adsorbed possibilities of the sites are equal,

(3) The site can adsorb only one molecule and express the monolayer adsorption

(4) The interaction between adsorbed molecules is impermissible,

(5) After partition equilibrium, the photocatalysis was started.

The Langmuir-Hinshelwood kinetics is generally utilized in the photocatalytic processes; the law is given by following equation:

$$r = -\frac{dC}{dt} = k_r\theta = \frac{k_r K_a C}{1 + K_a C}$$

The conventional linear transform of the Langmuir-Hinshelwood kinetics is

$$\frac{1}{r} = \frac{1}{k_r} + \frac{1}{k_r K_a} \times \frac{1}{C}$$

Where r is the initial rate of photocatalytic degradation for EDCs, k_r and K_a are the kinetic rate constant and partition coefficient, t is illumination time, C represents the concentration of the EDCs (equals to the concentration at the partition equilibrium). The value of k_r and K_a can be obtained from the linear plotted of $\frac{1}{r}$ versus $\frac{1}{C}$. For high concentrations of the pollutant ($K_a C \gg 1$), the photocatalysis reaction is followed zero-order rate equation. On the contrary, first-order kinetics describes the decomposition at very low initial concentration ($K_a C \ll 1$).

Table 4-6 and 4-7 show the initial decomposition rates of phenol and BPA with various initial concentrations in the presence of TOPO-capped TiO_2 and P25 and calculated kinetic rate constant and adsorption coefficient for Langmuir-Hinshelwood model. The photocatalytic initial rate increased with increasing initial concentration. The initial rates for phenol and BPA decomposition in the TOPO-capped TiO_2 system are 1.4 and 3.2 times, respectively, higher than those of Degussa P25. According to the Langmuir-Hinshelwood kinetic, the initial rate is related to the adsorption ability and photoactivity. Thus, using TOPO-capped TiO_2 as photocatalyst to decompose phenol and BPA has better ability than

P25.

In the case of phenol decomposition, TOPO-capped TiO_2 exhibit the higher K_a value (2.2×10^{-2} l/mg) than P25 (1.0×10^{-2} l/mg), due to the better partition ability between EDCs and the TOPO-capped TiO_2 catalyst.   However, the kinetic rate constant of TOPO-capped TiO_2 (7.3×10^{-2} ppm×g×min^{-1}×m^{-2}) is smaller than that of P25 (8.2×10^{-2} ppm×g×min^{-1}×m^{-2}).   This result is explained that the TOPO molecules occupied the active sites of TiO_2 surface leading to the lower photocatalytic activity.

In the cases of BPA decomposition, TOPO-capped TiO_2 exhibit the higher K_a and k_r value (6.4×10^{-2} l/mg, 1.4×10^{-1} ppm×g×min^{-1}×m^{-2}) than P25 (1.1×10^{-2} l/mg, 5.2×10^{-2} ppm×g×min^{-1}×m^{-2}), respectively.   The higher photocatalytic activity is correlated to the higher partition amounts of BPA on the surface of TOPO-capped TiO_2, and the better partition ability.   This result indicated that the organic modifier enhances the photoactivities via partitions.   BPA compounds can be decomposed by the photogenerated carriers immediately on the TOPO-capped TiO_2 surface owing to the better partition ability.

EPR results show the intensities of Ti^{4+}-O$^-$-Ti^{4+}-OH$^-$ and Ti^{4+}-O$_2^-$ radicals of TOPO-capped TiO_2 are higher than that of P25.   This result is presented that using the TOPO-capped TiO_2 as photocatalyst to decompose EDCs can inhibit the charge recombination.   And, the intensity of ·OH radical of TOPO-capped TiO_2 is smaller than that of P25.   According to the Langmuir-Hinshelwood kinetics model, the TOPO-capped TiO_2 has better photoactivity than P25 in this study.   Therefore, the photocatalytic mechanism of TOPO-capped TiO_2 mainly involves direct photodecomposition of EDCs by photo-generated charges rather by ·OH radicals which is normally occurred in the P25-based system.   In this study, the surface modification of TiO_2 with TOPO can promote the partition for hydrophobic molecules and inhibit the charges recombination, which can enhance photocatalytic degradation significantly.   Generally, after TiO_2 illumination, the photoexcited charge carriers migrate to the surface and react with surface adsorbed water and oxygen, then,

produce free radicals.　However, the pollutants close and adsorb to TiO_2 surface randomly.

　Furthermore, the number of the adsorption sites will increase after illumination.　The electronic properties of TiO_2 surface can be modified upon UV-illumination ($Ti^{4+} \rightarrow Ti^{3+}$; $O^{2-} \rightarrow O^{-}$), then EDCs can chemiadsorb on the charges at the TiO_2 surface.　The decomposed activity for EDCs increases with increasing the adsorption sites.　Similar result is reported by Parra et al., they found that the partition sites of TiO_2 surface will be change upon illumination.[89]
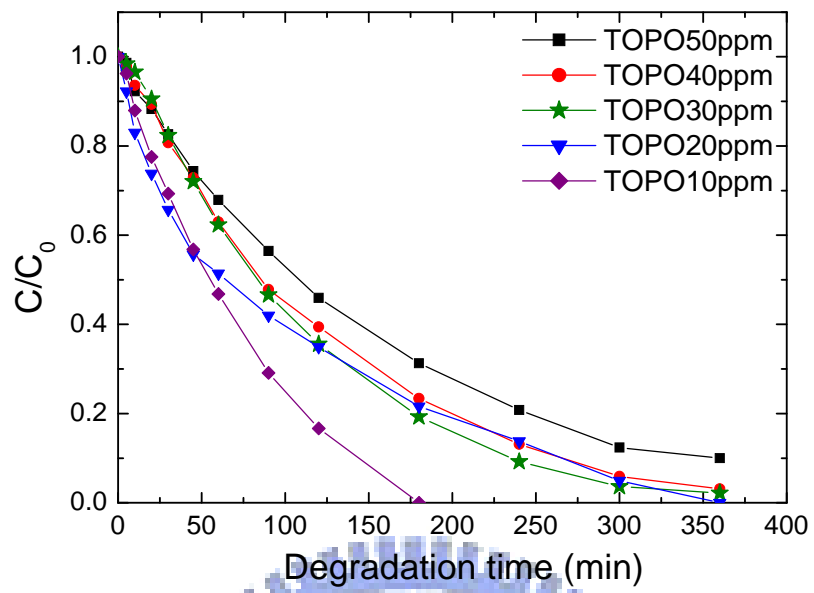
Figure 4- 16   Time courses of photodegradation of phenol with TOPO-capped TiO_2 and P25.
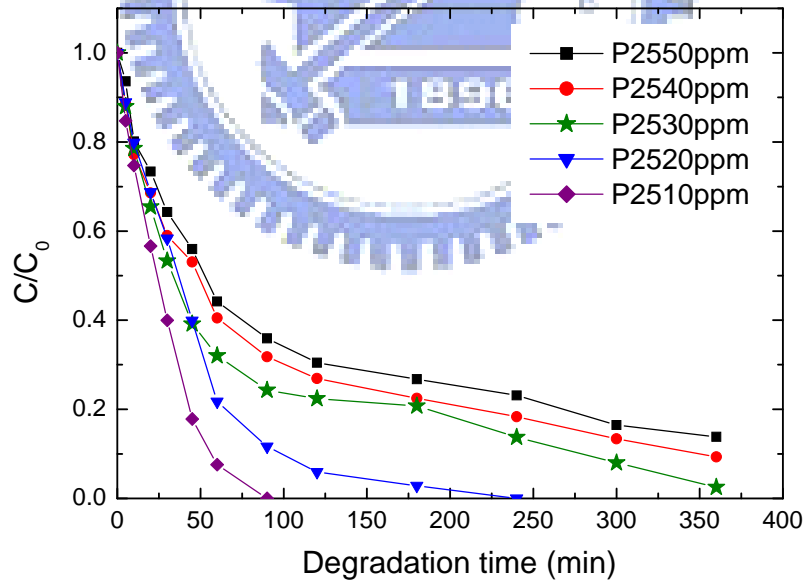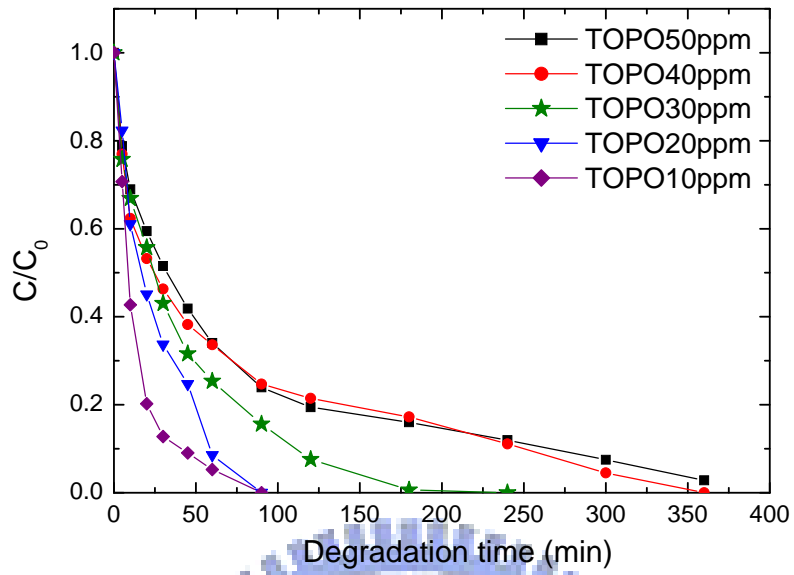
Figure 4- 17   Time courses of photodegradation of BPA with TOPO-capped TiO_2 and P25.

Table 4- 6　Apparent initial rates ($ppm \times g \times min^{-1} \times m^{-2}$) of various initial concentrations for phenol degradation with TOPO-capped TiO_2 and P25 and the kinetic rates constant and partition coefficients for Langmuir-Hinshelwood model.

Phenol	TOPO-capped TiO_2	P25
10 ppm	1.1×10^{-2}	7.5×10^{-3}
20 ppm	2.0×10^{-2}	1.2×10^{-2}
30 ppm	2.6×10^{-2}	1.9×10^{-2}
40 ppm	3.0×10^{-2}	2.2×10^{-2}
50 ppm	3.4×10^{-2}	3.1×10^{-2}
K_a (l/mg)	2.2×10^{-2}	1.0×10^{-2}
K_r ($ppm \times g \times min^{-1} \times m^{-2}$)	7.3×10^{-2}	8.2×10^{-2}
R^2	0.99	0.98

Table 4- 7　Apparent initial rates (ppm×g×min^{-1}×m^{-2}) of various initial concentrations for BPA degradation with TOPO-capped TiO$_2$ and P25 and the kinetic rate constants and partition coefficients for Langmuir-Hinshelwood model.

BPA	TOPO-capped TiO$_2$	P25
10 ppm	1.1×10^{-2}	4.9×10^{-3}
20 ppm	2.2×10^{-2}	7.6×10^{-3}
30 ppm	5.2×10^{-2}	1.3×10^{-2}
40 ppm	5.4×10^{-2}	1.8×10^{-2}
50 ppm	7.0×10^{-2}	2.0×10^{-2}
K_a (l/mg)	6.4×10^{-2}	1.1×10^{-2}
K_r (ppm×g×min^{-1}×m^{-2})	1.4×10^{-1}	5.2×10^{-2}
R^2	0.97	0.97

The much more hydrophobic EDCs, estrone (log K_{ow} = 3.13), were chose as my target compound in this study.   Furthermore, the photoactivities of TOPO-capped TiO$_2$ and P25 with respect to the decomposition of phenol (log K_{ow} = 1.46), BPA (log K_{ow} = 2.2) and estrone will be elucidated clearly.   Figure 4-18 shows the time courses of photodegradation of estrone by TOPO-capped TiO$_2$ or P25.   Estrone (with 5 ppm) can be degraded by TOPO-capped TiO$_2$ and P25 within 40 and 20 min illuminations, respectively.   Table 4-8 shows the initial photo-degradation rate of estrone under various initial concentrations in the presence of TOPO-capped TiO$_2$ and P25.   Photodegradation of estrone, 5 ppm, the initial rate of TOPO-capped TiO$_2$ (2.9×10^{-2} ppm$\times$g$\times$min$^{-1}\times$m^{-2}) is larger than that of P25 (1.8×10^{-2} ppm$\times$g$\times$min$^{-1}\times$m^{-2}), indicating the better photoactivity.   This result is resulted from the high affinity of TOPO-capped TiO$_2$ surface for estrone.

In the case of TOPO-capped TiO$_2$ system, the initial rate of estrone at an initial concentration of 5 ppm (2.9×10^{-2} ppm$\times$g$\times$min$^{-1}\times$m^{-2}) is larger than that of BPA at 10 ppm (1.1×10^{-2} ppm$\times$g$\times$min$^{-1}\times$m^{-2}).   According to the Langmuir-Hinshelwood kinetics model, the initial rate increases with increasing initial concentration.   Thus, it is supposed that the initial degradation rate of estrone at 10 ppm will much larger than phenol.   In summary, the photoactivity of TOPO-capped TiO$_2$ for estrone decomposition is higher than that of BPA and phenol.
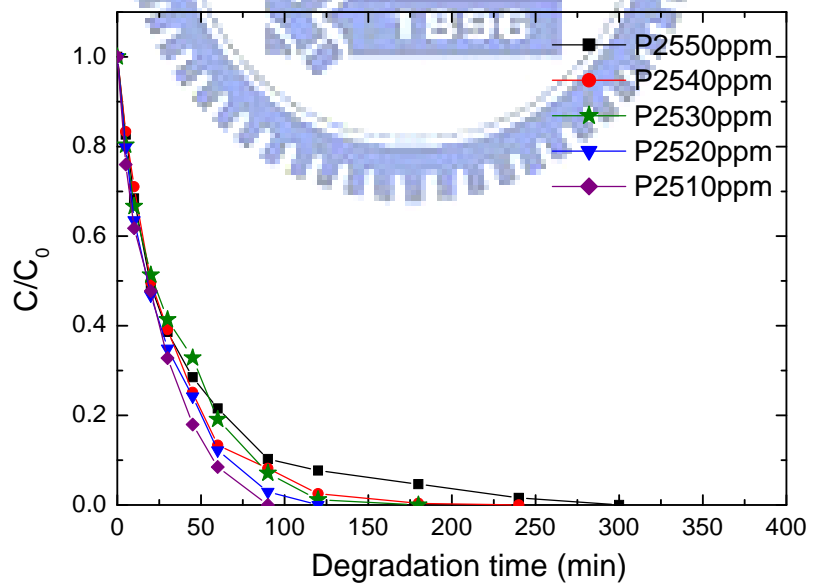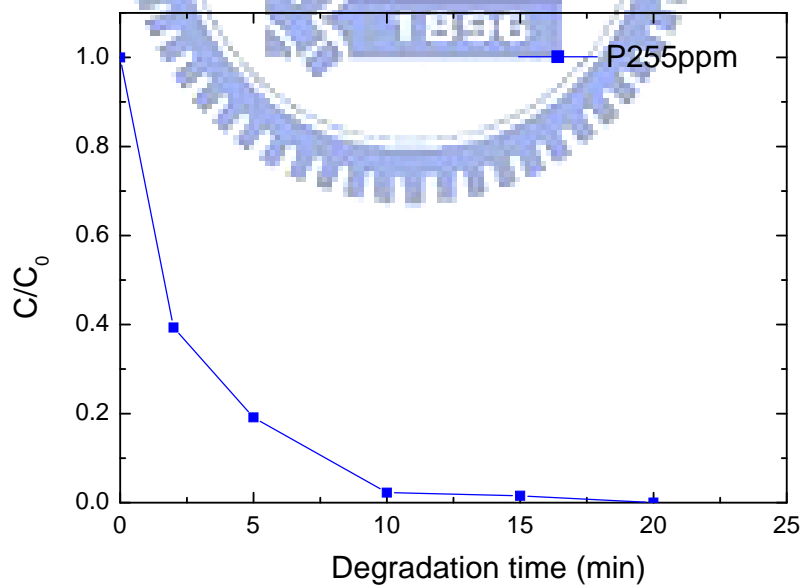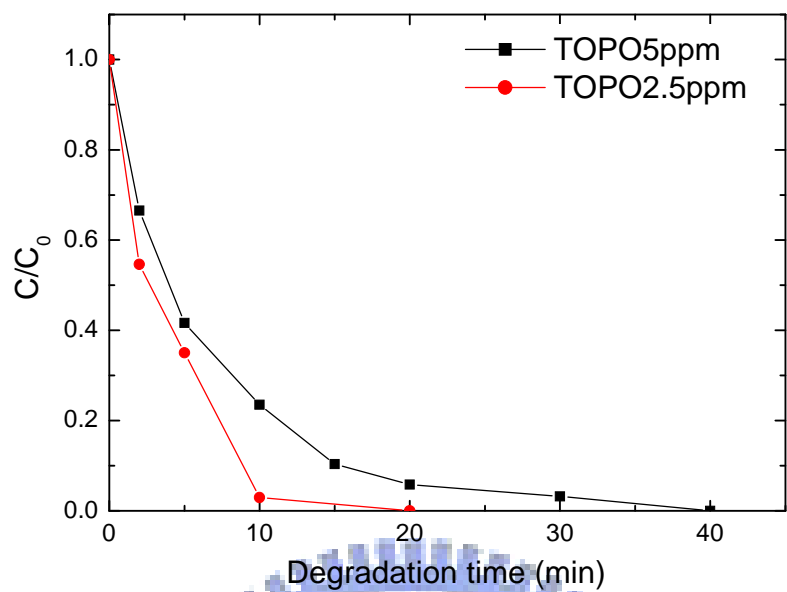
Figure 4- 18   Time courses of photodegradation of estrone with TOPO-capped TiO_2 and P25.

Table 4- 8   Apparent initial rates (ppm×g×min^{-1}×m^{-2}) of various initial concentrations for estrone degradation with TOPO-capped TiO$_2$ and P25.

	Estrone	
	TOPO-capped TiO$_2$	**P25**
2.5 ppm	1.2×10^{-2}	-
5 ppm	2.9×10^{-2}	1.8×10^{-2}

- : Not examined.

4.4.2   Competitive photocatalysis

TOPO-capped TiO$_2$ has hydrophobic character which has high affinity toward the EDCs. The rank of partition ability is estrone (3.79 l/mg) > BPA (5.9×10^{-2} l/mg) > phenol (4.4×10^{-2} l/mg) which due to the interaction between pollutants and TiO$_2$ surface.   Figure 4-19 shows the time courses of photodegradation in the presence of two kinds of EDCs with TOPO-capped TiO$_2$.   There are three batch photocatalytic systems containing the mixtures of phenol (10ppm)/ BPA (10ppm), phenol (10ppm)/ estrone (2.5ppm) and BPA (10ppm)/ estrone (2.5ppm).   In the phenol and BPA system, pollutants can be decomposed after 360 min illumination.   When the systems containing estrone, the phenol and BPA can be degrade totally after 300 min illumination.

Table 4-9 shows the apparent initial rates of the EDCs photodecomposition at various initial concentrations.   When the suspension contained phenol (10 ppm), BPA (10 ppm) and estrone (2.5 ppm) alone, the initial rates were 1.1×10^{-2}, 1.1×10^{-2} and 1.2×10^{-2} ppm×g×min^{-1}×m^{-2}, respectively.   In the case of phenol mixed with BPA, both of the initial rates of phenol (8.8×10^{-3} ppm×g×min^{-1}×m^{-2}) and BPA (1.1×10^{-2} ppm×g×min^{-1}×m^{-2}) are smaller than those of the systems which contain phenol (1.1×10^{-2} ppm×g×min^{-1}×m^{-2}) and BPA（1.1×10^{-2} ppm×g×min^{-1}×m^{-2}）alone.   In the case of phenol mixed with estrone, both of

the initial rates of phenol (1.0×10^{-2} ppm×g×min^{-1}×m^{-2}) and estrone (6.4×10^{-3} ppm×g×min^{-1}×m^{-2}) are much smaller than those of the systems which contain phenol (1.1×10^{-2} ppm×g×min^{-1}×m^{-2}) and estrone（1.2×10^{-2} ppm×g×min^{-1}×m^{-2}）alone. In the case of BPA mixed with estrone, both of the initial rates of BPA (4.9×10^{-3} ppm×g×min^{-1}×m^{-2}) and estrone (4.7×10^{-3} ppm×g×min^{-1}×m^{-2}) are smaller than those of the systems which contain BPA (1.1×10^{-2} ppm×g×min^{-1}×m^{-2}) and estrone (1.2×10^{-2} ppm×g×min^{-1}×m^{-2}) alone. The initial rates of aqueous solutions containing pollutants alone were larger than those of competitive systems. This is due to the competitive effects will inhibit the pollutants adsorbed on TiO$_2$ surface significantly. Then, the decomposed reactions of EDCs are suppressed.
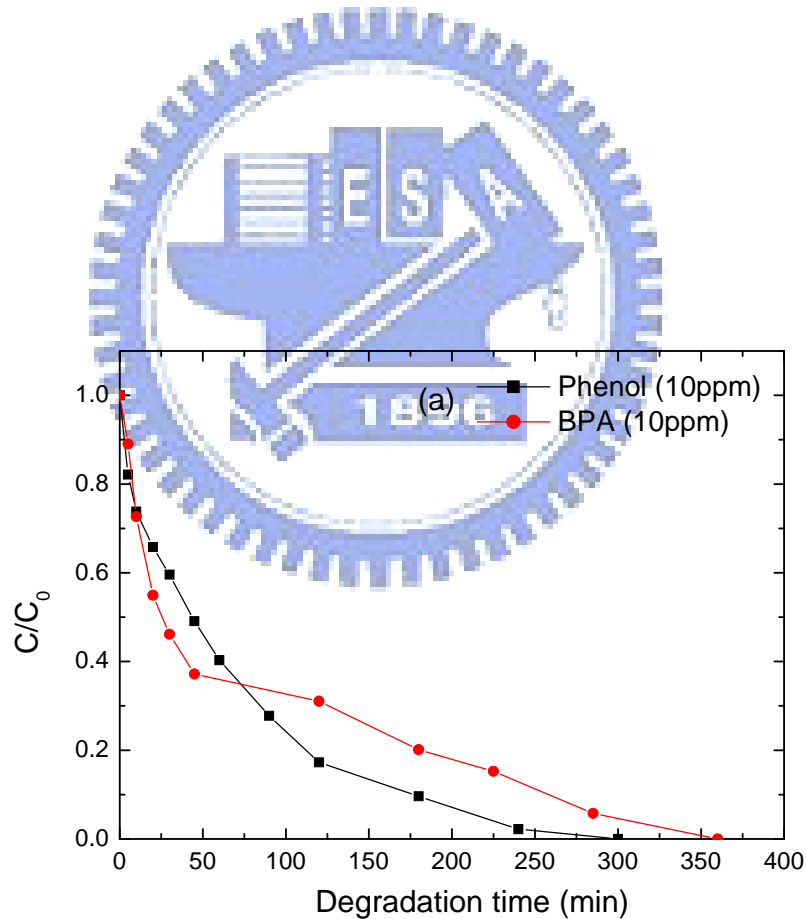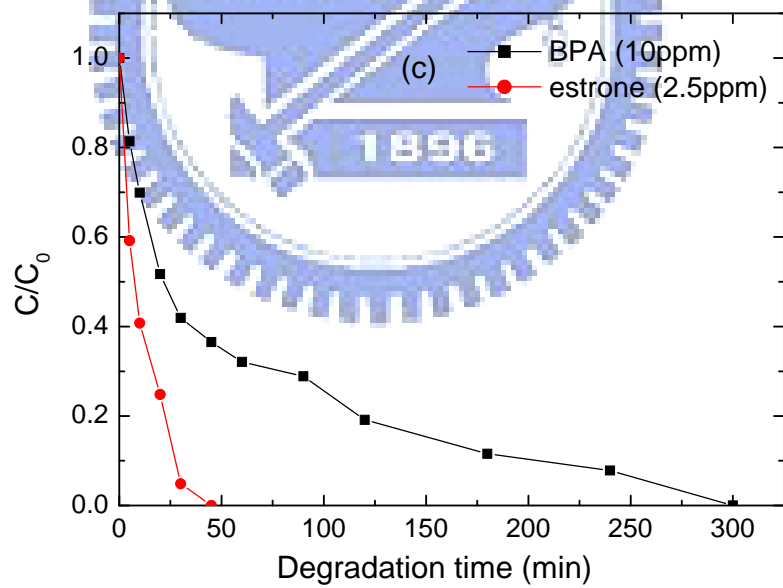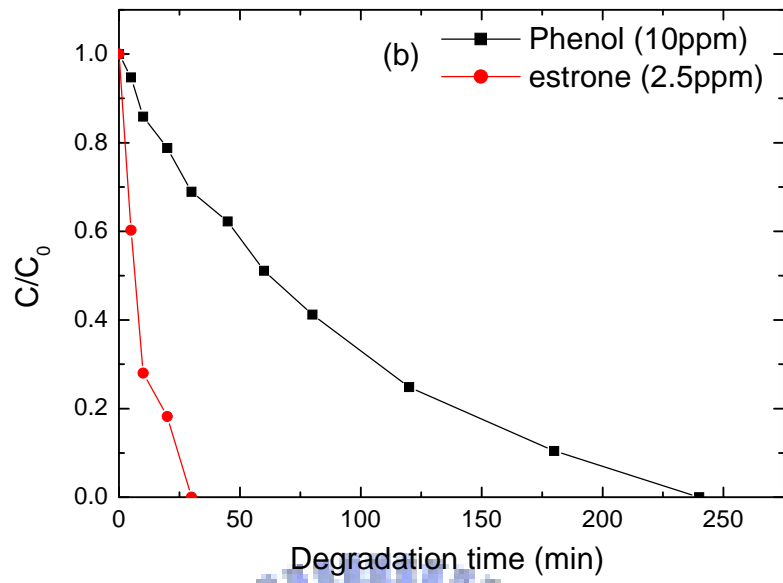
Figure 4- 19   Time course of photodegradation in the presence of two kinds of EDCs with TOPO-capped TiO$_2$ for mixing (a) phenol (10ppm) and BPA (10ppm), (b) phenol (10ppm) and estrone(2.5ppm) and (c) BPA (10ppm) and estrone (2.5ppm).

Table 4- 9   Apparent initial rates (ppm×g×min^{-1}×m^{-2}) of various initial concentrations for competitive degradation with TOPO-capped TiO$_2$.

		Competition	**Alone**
phenol + BPA	Phenol (10ppm)	8.8×10^{-3}	1.1×10^{-2}
	BPA (10ppm)	1.1×10^{-2}	1.1×10^{-2}
phenol + estrone	Phenol (10ppm)	1.0×10^{-2}	1.1×10^{-2}
	Estrone (2.5ppm)	6.4×10^{-3}	1.2×10^{-2}
BPA + estrone	BPA (10ppm)	4.9×10^{-3}	1.1×10^{-2}
	Estrone (2.5ppm)	4.7×10^{-3}	1.2×10^{-2}

4.4.3   After photocatalysis

In the view of understanding the destruction of surface property of TOPO-capped TiO$_2$ after photocatalysis, XPS was used to detect the composition of TiO$_2$ surface.   The atomic ratios of P/C and P/Ti from XPS spectroscopy were shown in Table 4-10.   Before photocatalysis, the TOPO-capped TiO$_2$ had a lower C/P ratio of 13.2 which was smaller than stoichiometric ratio of 24.0.   The result illustrates that TOPO molecules were destroyed by high temperature during preparation course.   After photocatalysis of EDCs, C/P ratio decrease significantly.   The C/P ratios of photodegradation of phenol for 2.5 hours, BPA for 1.5 hours and estrone for 40 minutes declined to 7.86, 6.60 and 8.64.   The TOPO is partially decomposed after photocatalysis in this research.   At the same time, TOPO-capped TiO$_2$ also has lots of carbon on the surface maintained the hydrophobic characteristic.   It should be concluded that this photocatalyst is highly potential to be used to adsorb and photodecompose hydrophobic pollutants.

Table 4- 10   The TOPO-capped TiO_2 powder has been damaged after photocatalysis.

	n_P/n_C	n_P/n_{Ti}
Pure TOPO-capped TiO₂ without reaction	13.2	0.36
Phenol after 2.5 hours reaction	7.86	0.5
BPA after 1.5 hours reaction	6.60	0.5
Estrone after 40 minutes reaction	8.64	0.42

Chapter 5. Conclusions

TOPO-capped TiO_2 have been successfully synthesized via a non-hydrolytic sol-gel process. In this study, TOPO-capped TiO_2 catalysts have clearly demonstrated to have excellent photoactivies toward EDCs decompositions. A higher partition efficiency of EDCs on TiO_2 surface was due to the TOPO modification. Estrone with the highest log K_{ow} value exhibited the largest partition amounts on the TOPO-capped TiO_2 compared with phenol and BPA. Moreover, there are three steps affect the decomposed reaction: one is partition, another is that adsorbed EDCs diffuse to the TiO_2 surface, the other is surface reaction. The partition activity contributes to the acceleration of the EDCs decomposition. For this reason, surface modification resulted in increasing the surface coverage of pollutants, thus enhanced the photocatalytic rate. According to the EPR results, the Ti^{4+}-O^--Ti^{4+}-OH^- adducts for TOPO-capped TiO_2 is stronger than that of P25. These results reveal TOPO can facilitate the transfer of photogenerated charges from TiO_2 to the adsorbed EDCs. The charges at the TiO_2 surface can chemiadsorb EDCs significantly upon UV-illumination. Therefore, the EDCs photodecomposition of TOPO-capped TiO_2 mainly occurs by photoinduced charges rather by $\cdot$OH radicals which is normally occurred in the P25-based system. After photocatalysis of phenol, BPA and estrone, the phosphorus atoms still chelate on TiO_2 surface. In addition, lots of carbon atoms are still remained on the TiO_2 surface, revealing the reusable properties of the TOPO-capped TiO_2 for next photocatalytic runs.

References

1.   Roepke, T. A.; Snyder, M. J.; Cherr, G. N., Estradiol and endocrine disrupting compounds adversely affect development of sea urchin embryos at environmentally relevant concentrations. *Aquatic Toxicology* **2005,** 71, (2), 155-173.

2.   Jorgensen, M.; Vendelbo, B.; Skakkebaek, N. E.; Leffers, H., Assaying estrogenicity by quantitating the expression levels of endogenous estrogen-regulated genes. *Environmental Health Perspectives* **2000,** 108, (5), 403-412.

3.   Lee, H. B.; Peart, T. E.; Svoboda, M. L., Determination of endocrine-disrupting phenols, acidic pharmaceuticals, and personal-care products in sewage by solid-phase extraction and gas chromatography-mass spectrometry. *Journal of Chromatography A* **2005,** 1094, (1-2), 122-129.

4.   Colborn, T.; Saal, F. S. V.; Soto, A. M., Developmental Effects of Endocrine-Disrupting Chemicals in Wildlife and Humans. *Environmental Health Perspectives* **1993,** 101, (5), 378-384.

5.   Depledge, M. H.; Billinghurst, Z., Ecological significance of endocrine disruption in marine invertebrates. *Marine Pollution Bulletin* **1999,** 39, (1-12), 32-38.

6.   Westerhoff, P.; Yoon, Y.; Snyder, S.; Wert, E., Fate of endocrine-disruptor, pharmaceutical, and personal care product chemicals during simulated drinking water treatment processes. *Environmental Science & Technology* **2005,** 39, (17), 6649-6663.

7.   Nakada, N.; Shinohara, H.; Murata, A.; Kiri, K.; Managaki, S.; Sato, N.; Takada, H., Removal of selected pharmaceuticals and personal care products (PPCPs) and endocrine-disrupting chemicals (EDCs) during sand filtration and ozonation at a municipal sewage treatment plant. *Water Research* **2007,** 41, (19), 4373-4382.

8.   Anpo, M.; Takeuchi, M., The design and development of highly reactive titanium oxide photocatalysts operating under visible light irradiation. *Journal of Catalysis* **2003,** 216, (1-2), 505-516.

9.   Ding, Z.; Lu, G. Q.; Greenfield, P. F., Role of the crystallite phase of TiO2 in heterogeneous photocatalysis for phenol oxidation in water. *Journal of Physical Chemistry B* **2000,** 104, (19), 4815-4820.

10. Herrmann, J. M., Heterogeneous photocatalysis: fundamentals and applications to the removal of various types of aqueous pollutants. *Catalysis Today* **1999,** 53, (1), 115-129.

11. Ohko, Y.; Ando, I.; Niwa, C.; Tatsuma, T.; Yamamura, T.; Nakashima, T.; Kubota, Y.; Fujishima, A., Degradation of bisphenol A in water by TiO2 photocatalyst. *Environmental Science & Technology* **2001,** 35, (11), 2365-2368.

12. Kurinobu, S.; Tsurusaki, K.; Natui, Y.; Kimata, M.; Hasegawa, M., Decomposition of pollutants in wastewater using magnetic photocatalyst particles. *Journal of Magnetism and*

Magnetic Materials **2007,** 310, (2), E1025-E1027.

13. Kohtani, S.; Hiro, J.; Yamamoto, N.; Kudo, A.; Tokumura, K.; Nakagaki, R., Adsorptive and photocatalytic properties of Ag-loaded BiVO4 on the degradation of 4-n-alkylphenols under visible light irradiation. *Catalysis Communications* **2005,** 6, (3), 185-189.

14. Yue, B.; Zhou, Y.; Xu, J. Y.; Wu, Z. Z.; Zhang, X. A.; Zou, Y. F.; Jin, S. L., Photocatalytic degradation of aqueous 4-chlorophenol by silica-immobilized polyoxometalates. *Environmental Science & Technology* **2002,** 36, (6), 1325-1329.

15. Kasahara, T.; Inumaru, K.; Yamanaka, S., Enhanced photocatalytic decomposition of nonylphenol polyethoxylate by alkyl-grafted TiO2-MCM-41 organic-inorganic nanostructure. *Microporous and Mesoporous Materials* **2004,** 76, (1-3), 123-130.

16. Andrzejewska, A.; Krysztafkiewicz, A.; Jesionowski, T., Adsorption of organic dyes on the aminosilane modified TiO2 surface. *Dyes and Pigments* **2004,** 62, (2), 121-130.

17. Tryba, B.; Tsumura, T.; Janus, M.; Morawski, A. W.; Inagaki, M., Carbon-coated anatase: adsorption and decomposition of phenol in water. *Applied Catalysis B-Environmental* **2004,** 50, (3), 177-183.

18. Noguchi, H.; Nakajima, A.; Watanabe, T.; Hashimoto, K., Design of a photocatalyst for bromate decomposition: Surface modification of TiO2 by pseudo-boehmite. *Environmental Science & Technology* **2003,** 37, (1), 153-157.

19. Yuan, Q. Z.; Ravikrishna, R.; Valsaraj, K. T., Reusable adsorbents for dilute solution separation. 5. Photodegradation of organic compounds on surfactant-modified titania. *Separation and Purification Technology* **2001,** 24, (1-2), 309-318.

20. Li, S. X.; Zheng, F. Y.; Cai, W. L.; Han, A. Q.; Xie, Y. K., Surface modification of nanometer size TiO2 with salicylic acid for photocatalytic degradation of 4-nitrophenol. *Journal of Hazardous Materials* **2006,** 135, (1-3), 431-436.

21. Simakov, S. A.; Tsur, Y., Surface stabilization of nano-sized titanium dioxide: Improving the colloidal stability and the sintering morphology. *Journal of Nanoparticle Research* **2007,** 9, (3), 403-417.

22. Ou, Y.; Lin, J. D.; Zou, H. M.; Liao, D. W., Effects of surface modification of TiO2 with ascorbic acid on photocatalytic decolorization of an azo dye reactions and mechanisms. *Journal of Molecular Catalysis a-Chemical* **2005,** 241, (1-2), 59-64.

23. Yu, J. C.; Ho, W. K.; Yu, J. G.; Hark, S. K.; Iu, K., Effects of trifluoroacetic acid modification on the surface microstructures and photocatalytic activity of mesoporous TiO2 thin films. *Langmuir* **2003,** 19, (9), 3889-3896.

24. Makarova, O. V.; Rajh, T.; Thurnauer, M. C.; Martin, A.; Kemme, P. A.; Cropek, D., Surface modification of TiO2 nanoparticles for photochemical reduction of nitrobenzene. *Environmental Science & Technology* **2000,** 34, (22), 4797-4803.

25. Xagas, A. P.; Bernard, M. C.; Hugot-Le Goff, A.; Spyrellis, N.; Loizos, Z.; Falaras, P., Surface modification and photosensitisation of TiO2 nanocrystalline films with ascorbic acid.

Journal of Photochemistry and Photobiology a-Chemistry **2000,** 132, (1-2), 115-120.

26. Jiang, D.; Xu, Y.; Hou, B.; Wu, D.; Sun, Y. H., Synthesis of visible light-activated TiO2 photocatalyst via surface organic modification. *Journal of Solid State Chemistry* **2007,** 180, (5), 1787-1791.

27. Chang, S. M.; Doong, R. A., Characterization of Zr-doped TiO2 nanocrystals prepared by a nonhydrolytic sol-gel method at high temperatures. *Journal of Physical Chemistry B* **2006,** 110, (42), 20808-20814.

28. Trentler, T. J.; Denler, T. E.; Bertone, J. F.; Agrawal, A.; Colvin, V. L., Synthesis of TiO2 nanocrystals by nonhydrolytic solution-based reactions. *Journal of the American Chemical Society* **1999,** 121, (7), 1613-1614.

29. Zhang, L. F.; Kanki, T.; Sano, N.; Toyoda, A., Pathways and kinetics on photocatalytic destruction of aqueous phenol. *Environmental Monitoring and Assessment* **2006,** 115, (1-3), 395-403.

30. Ichinose, H.; Terasaki, M.; Katsuki, H., Properties of peroxotitanium acid solution and peroxo-modified anatase sol derived from peroxotitanium hydrate. *Journal of Sol-Gel Science and Technology* **2001,** 22, (1-2), 33-40.

31. Litter, M. I., Heterogeneous photocatalysis - Transition metal ions in photocatalytic systems. In *Applied Catalysis B-Environmental*, 1999; Vol. 23, pp 89-114.

32. Linsebigler, A. L.; Lu, G. Q.; Yates, J. T., Photocatalysis on Tio2 Surfaces - Principles, Mechanisms, and Selected Results. *Chemical Reviews* **1995,** 95, (3), 735-758.

33. Serpone, N.; Sauve, G.; Koch, R.; Tahiri, H.; Pichat, P.; Piccinini, P.; Pelizzetti, E.; Hidaka, H., Standardization protocol of process efficiencies and activation parameters in heterogeneous photocatalysis: Relative photonic efficiencies zeta(r). *Journal of Photochemistry and Photobiology a-Chemistry* **1996,** 94, (2-3), 191-203.

34. Chen, D. W.; Ray, A. K., Photodegradation kinetics of 4-nitrophenol in TiO2 suspension. *Water Research* **1998,** 32, (11), 3223-3234.

35. Park, N. G.; van de Lagemaat, J.; Frank, A. J., Comparison of dye-sensitized rutile- and anatase-based TiO2 solar cells. *Journal of Physical Chemistry B* **2000,** 104, (38), 8989-8994.

36. Lu, Z. L.; Lindner, E.; Mayer, H. A., Applications of sol-gel-processed interphase catalysts. *Chemical Reviews* **2002,** 102, (10), 3543-3577.

37. Arnal, P.; Corriu, R. J. P.; Leclercq, D.; Mutin, P. H.; Vioux, A., A solution chemistry study of nonhydrolytic sol-gel routes to titania. *Chemistry of Materials* **1997,** 9, (3), 694-698.

38. Vioux, A., Nonhydrolytic sol-gel routes to oxides. *Chemistry of Materials* **1997,** 9, (11), 2292-2299.

39. Andrianainarivelo, M.; Corriu, R. J. P.; Leclercq, D.; Mutin, P. H.; Vioux, A., Non-hydrolytic sol-gel process: Zirconium titanate gels. *Journal of Materials Chemistry* **1997,** 7, (2), 279-284.

40. Andrianainarivelo, M.; Corriu, R. J. P.; Leclercq, D.; Mutin, P. H.; Vioux, A.,

Nonhydrolytic sol-gel process: Aluminum titanate gels. *Chemistry of Materials* **1997,** 9, (5), 1098-1102.

41.   Andrianainarivelo, M.; Corriu, R. J. P.; Leclercq, D.; Mutin, P. H.; Vioux, A., Nonhydrolytic Sol-Gel process: Aluminium and zirconium titanate gels. *Journal of Sol-Gel Science and Technology* **1997,** 8, (1-3), 89-93.

42.   Pan, D. C.; Zhao, N. N.; Wang, Q.; Jiang, S. C.; Ji, X. L.; An, L. J., Facile synthesis and characterization of luminescent TiO2 nanocrystals. *Advanced Materials* **2005,** 17, (16), 1991-+.

43.   Rockenberger, J.; Scher, E. C.; Alivisatos, A. P., A new nonhydrolytic single-precursor approach to surfactant-capped nanocrystals of transition metal oxides. *Journal of the American Chemical Society* **1999,** 121, (49), 11595-11596.

44.   West, L. L. H. a. J. K., The Sol-Gel Prosess. *Chemical Reviews* **1990,** 90, (1), 33-72.

45.   钱力鹏, 侯., 李亚利, 非水體系合成不同形態的二氧化鈦納米晶. **2007**.

46.   Korosi, L.; Dekany, I., Preparation and investigation of structural and photocatalytic properties of phosphate modified titanium dioxide. *Colloids and Surfaces a-Physicochemical and Engineering Aspects* **2006,** 280, (1-3), 146-154.

47.   Korosi, L.; Papp, S.; Bertoti, I.; Dekany, I., Surface and bulk composition, structure, and photocatalytic activity of phosphate-modified TiO2. *Chemistry of Materials* **2007,** 19, (19), 4811-4819.

48.   Yu, J. C.; Zhang, L. Z.; Zheng, Z.; Zhao, J. C., Synthesis and characterization of phosphated mesoporous titanium dioxide with high photocatalytic activity. *Chemistry of Materials* **2003,** 15, (11), 2280-2286.

49.   Huang, D.; Luo, G. S.; Wang, Y. J., Using phosphoric acid as a catalyst to control the structures of mesoporous titanium dioxide materials. *Microporous and Mesoporous Materials* **2005,** 84, (1-3), 27-33.

50.   Lee, J. M.; Kim, M. S.; Kim, B. W., Photodegradation of bisphenol-A with TiO2 immobilized on the glass tubes including the UV light lamps. *Water Research* **2004,** 38, (16), 3605-3613.

51.   Tai, C.; Jiang, G. B.; Liu, J. F.; Zhou, Q. F.; Liu, J. Y., Rapid degradation of bisphenol A using air as the oxidant catalyzed by polynuclear phthalocyanine complexes under visible light irradiation. *Journal of Photochemistry and Photobiology a-Chemistry* **2005,** 172, (3), 275-282.

52.   Bolger, R.; Wiese, T. E.; Ervin, K.; Nestich, S.; Checovich, W., Rapid screening of environmental chemicals for estrogen receptor binding capacity. *Environmental Health Perspectives* **1998,** 106, (9), 551-557.

53.   Lagana, A.; Bacaloni, A.; De Leva, I.; Faberi, A.; Fago, G.; Marino, A., Analytical methodologies for determining the occurrence of endocrine disrupting chemicals in sewage treatment plants and natural waters. *Analytica Chimica Acta* **2004,** 501, (1), 79-88.

54. Ankley, G.; Mihaich, E.; Stahl, R.; Tillitt, D.; Colborn, T.; McMaster, S.; Miller, R.; Bantle, J.; Campbell, P.; Denslow, N.; Dickerson, R.; Folmar, L.; Fry, M.; Giesy, J.; Gray, L. E.; Guiney, P.; Hutchinson, T.; Kennedy, S.; Kramer, V.; LeBlanc, G.; Mayes, M.; Nimrod, A.; Patino, R.; Peterson, R.; Purdy, R.; Ringer, R.; Thomas, P.; Touart, L.; Van der Kraak, G.; Zacharewski, T., Overview of a workshop on screening methods for detecting potential (anti-) estrogenic/androgenic chemicals in wildlife. *Environmental Toxicology and Chemistry* **1998,** 17, (1), 68-87.

55. Wang, G. H.; Wu, F.; Zhang, X.; Luo, M. D.; Deng, N. S., Enhanced TiO2 photocatalytic degradation of bisphenol A by beta-cyclodextrin in suspended solutions. *Journal of Photochemistry and Photobiology a-Chemistry* **2006,** 179, (1-2), 49-56.

56. Terasaki, M.; Shiraishi, F.; Nishikawa, T.; Edmonds, J. S.; Morita, M.; Makino, M., Estrogenic activity of impurities in industrial grade bisphenol A. *Environmental Science & Technology* **2005,** 39, (10), 3703-3707.

57. Kaneco, S.; Rahman, M. A.; Suzuki, T.; Katsumata, H.; Ohta, K., Optimization of solar photocatalytic degradation conditions of bisphenol A in water using titanium dioxide. *Journal of Photochemistry and Photobiology a-Chemistry* **2004,** 163, (3), 419-424.

58. Watanabe, N.; Horikoshi, S.; Kawabe, H.; Sugie, Y.; Zhao, J. C.; Hidaka, H., Photodegradation mechanism for bisphenol A at the TiO2/H2O interfaces. *Chemosphere* **2003,** 52, (5), 851-859.

59. Sun, B.; Vorontsov, A. V.; Smirniotis, P. G., Role of platinum deposited on TiO2 in phenol photocatalytic oxidation. *Langmuir* **2003,** 19, (8), 3151-3156.

60. Chiang, K.; Lim, T. M.; Tsen, L.; Lee, C. C., Photocatalytic degradation and mineralization of bisphenol A by TiO2 and platinized TiO2. *Applied Catalysis a-General* **2004,** 261, (2), 225-237.

61. Zhang, L. F.; Kanki, T.; Sano, N.; Toyoda, A., Development of TiO2 photocatalyst reaction for water purification. *Separation and Purification Technology* **2003,** 31, (1), 105-110.

62. Nahar, M. S.; Hasegawa, K.; Kagaya, S.; Kuroda, S., Comparative assessment of the efficiency of Fe-doped TiO2 prepared by two doping methods and photocatalytic degradation of phenol in domestic water suspensions. *Science and Technology of Advanced Materials* **2007,** 8, (4), 286-291.

63. Yuan, Z. H.; Jia, J. H.; Zhang, L. D., Influence of co-doping of Zn(II) plus Fe(III) on the photocatalytic activity of TiO2 for phenol degradation. *Materials Chemistry and Physics* **2002,** 73, (2-3), 323-326.

64. Dobosz, A.; Sobczynski, A., The influence of silver additives on titania photoactivity in the photooxidation of phenol. *Water Research* **2003,** 37, (7), 1489-1496.

65. Tryba, B.; Morawski, A. W.; Inagaki, M.; Toyoda, M., The kinetics of phenol decomposition under UV irradiation with and without H2O2 on TiO2, Fe-TiO2 and

Fe-C-TiO2 photocatalysts. *Applied Catalysis B-Environmental* **2006,** 65, (1-2), 86-92.

66. Tryba, B.; Toyoda, M.; Morawski, A. W.; Inagaki, M., Modification of carbon-coated TiO2 by iron to increase adsorptivity and photoactivity for phenol. *Chemosphere* **2005,** 60, (4), 477-484.

67. Colon, G.; Sanchez-Espana, J. M.; Hidalgo, M. C.; Navio, J. A., Effect of TiO2 acidic pre-treatment on the photocatalytic properties for phenol degradation. *Journal of Photochemistry and Photobiology a-Chemistry* **2006,** 179, (1-2), 20-27.

68. Sobczynski, A.; Duczmal, L.; Zmudzinski, W., Phenol destruction by photocatalysis on TiO2: an attempt to solve the reaction mechanism. *Journal of Molecular Catalysis a-Chemical* **2004,** 213, (2), 225-230.

69. Venkatachalam, N.; Palanichamy, M.; Arabindoo, B.; Murugesan, V., Alkaline earth metal doped nanoporous TiO2 for enhanced photocatalytic mineralisation of bisphenol-A. *Catalysis Communications* **2007,** 8, (7), 1088-1093.

70. Coleman, H. M.; Chiang, K.; Amal, R., Effects of Ag and Pt on photocatalytic degradation of endocrine disrupting chemicals in water. *Chemical Engineering Journal* **2005,** 113, (1), 65-72.

71. Li, X. Z.; He, C.; Graham, N.; Xiong, Y., Photoelectrocatalytic degradation of bisphenol A in aqueous solution using a Au-TiO2/ITO film. *Journal of Applied Electrochemistry* **2005,** 35, (7), 741-750.

72. Xie, Y. B.; Li, X. Z., Degradation of bisphenol A in aqueous solution by H2O2-assisted photoelectrocatalytic oxidation. *Journal of Hazardous Materials* **2006,** 138, (3), 526-533.

73. Katsumata, H.; Kawabe, S.; Kaneco, S.; Suzuki, T.; Ohta, K., Degradation of bisphenol A in water by the photo-Fenton reaction. *Journal of Photochemistry and Photobiology a-Chemistry* **2004,** 162, (2-3), 297-305.

74. Ioan, I.; Wilson, S.; Lundanes, E.; Neculai, A., Comparison of Fenton and sono-Fenton bisphenol A degradation. *Journal of Hazardous Materials* **2007,** 142, (1-2), 559-563.

75. Gultekin, I.; Ince, N. H., Ultrasonic destruction of bisphenol-A: The operating parameters. *Ultrasonics Sonochemistry* **2008,** 15, (4), 524-529.

76. Shareef, A.; Angove, M. J.; Wells, J. D.; Johnson, B. B., Aqueous solubilities of estrone, 17 beta-estradiol, 17 alpha-ethynylestradiol, and bisphenol A. *Journal of Chemical and Engineering Data* **2006,** 51, (3), 879-881.

77. Zhang, Y.; Zhou, J. L.; Ning, B., Photodegradation of estrone and 17 beta-estradiol in water. *Water Research* **2007,** 41, (1), 19-26.

78. Sauer, T.; Neto, G. C.; Jose, H. J.; Moreira, R. F. P. M., Kinetics of photocatalytic degradation of reactive dyes in a TiO2 slurry reactor. *Journal of Photochemistry and Photobiology a-Chemistry* **2002,** 149, (1-3), 147-154.

79. Mizuguchi, T.; Shibayama, Y.; Mitamura, K.; Shimada, K., Contribution of glucuronic acid and sulfonic acid moieties during photocatalytic degradation of estrogen conjugates.

Journal of Health Science **2005,** 51, (4), 447-452.

80. Coleman, H. M.; Routledge, E. J.; Sumpter, J. P.; Eggins, B. R.; Byrne, J. A., Rapid loss of estrogenicity of steroid estrogens by UVA photolysis and photocatalysis over an immobilised titanium dioxide catalyst. *Water Research* **2004,** 38, (14-15), 3233-3240.

81. Kumar, K. N. P.; Keizer, K.; Burggraaf, A. J., Textural Evolution and Phase-Transformation in Titania Membranes .1. Unsupported Membranes. *Journal of Materials Chemistry* **1993,** 3, (11), 1141-1149.

82. Lacombe, S.; Cardy, H.; Soggiu, N.; Blanc, S.; Habib-Jiwan, J. L.; Soumillion, J. P., Diffuse reflectance UV-Visible spectroscopy for the qualitative and quantitative study of chromophores adsorbed or grafted on silica. *Microporous and Mesoporous Materials* **2001,** 46, (2-3), 311-325.

83. Morrison, C.; Kiwi*, J., Preparation and characterization of TiO2–SiO2 aerosil colloidal mixed dispersions. *J. Chem. Soc., Faraday Trans. 1* **1989,** 85, (1019-1198).

84. Nakaoka, Y.; Nosaka, Y., ESR Investigation into the effects of heat treatment and crystal structure on radicals produced over irradiated TiO2 powder. *Journal of Photochemistry and Photobiology a-Chemistry* **1997,** 110, (3), 299-305.

85. Coronado, J. M.; Maira, A. J.; Conesa, J. C.; Yeung, K. L.; Augugliaro, V.; Soria, J., EPR study of the surface characteristics of nanostructured TiO2 under UV irradiation. *Langmuir* **2001,** 17, (17), 5368-5374.

86. Billik, P.; Plesch, G.; Brezova, V.; Kuchta, L.; Valko, M.; Mazur, M., Anatase TiO2 nanocrystals prepared by mechanochemical synthesis and their photochemical activity studied by EPR spectroscopy. *Journal of Physics and Chemistry of Solids* **2007,** 68, (5-6), 1112-1116.

87. Li, H.; Van Berlo, D.; Shi, T.; Spelt, G.; Knaapen, A. M.; Borm, P. J. A.; Albrecht, C.; Schins, R. P. F., Curcumin protects against cytotoxic and inflammatory effects of quartz particles but causes oxidative DNA damage in a rat lung epithelial cell line. *Toxicology and Applied Pharmacology* **2008,** 227, (1), 115-124.

88. Madden, K. P.; Taniguchi, H., The role of the DMPO-hydrated electron spin adduct in DMPO-(OH)-O-center dot spin trapping. *Free Radical Biology and Medicine* **2001,** 30, (12), 1374-1380.

89. Parra, S.; Olivero, J.; Pulgarin, C., Relationships between physicochemical properties and photoreactivity of four biorecalcitrant phenylurea herbicides in aqueous TiO2 suspension. *Applied Catalysis B-Environmental* **2002,** 36, (1), 75-85.

Appendix A.   Experimental parameters

Appendix A- 1　Operational parameters of XRPD.

Scan range (degree)	Sampling width (degree)	Scan speed (degree/min)	Measurement type	Voltage (kV)	Current (mA)
20-90 degree	0.02	4.0	Ordinary (without background)	30.0	20.0

Appendix A- 2　Operational parameters of XPS.

Mode	Binding energy	Pass energy	Anode	Step size	Time/steps
Survey	1200-0 eV	23.5 eV	Al	1.0 eV	50 ms
Multiplex	Depending on element	23.5 eV	Al	0.1 eV	50 ms

Appendix A- 3　Detail operational parameters of XPS in multiplex.

Element	Pass energy (eV)	Step size (eV)	Scans	BE range	ASF
P_{2p}	23.5	0.1	80	127-147	0.486
C_{1s}	23.5	0.1	40	280-300	0.296
O_{1s}	23.5	0.1	30	525-545	0.711
Ti_{2P}	23.5	0.1	25	451-476	2.001

Appendix A- 4   Operational parameters of UV-Visible.

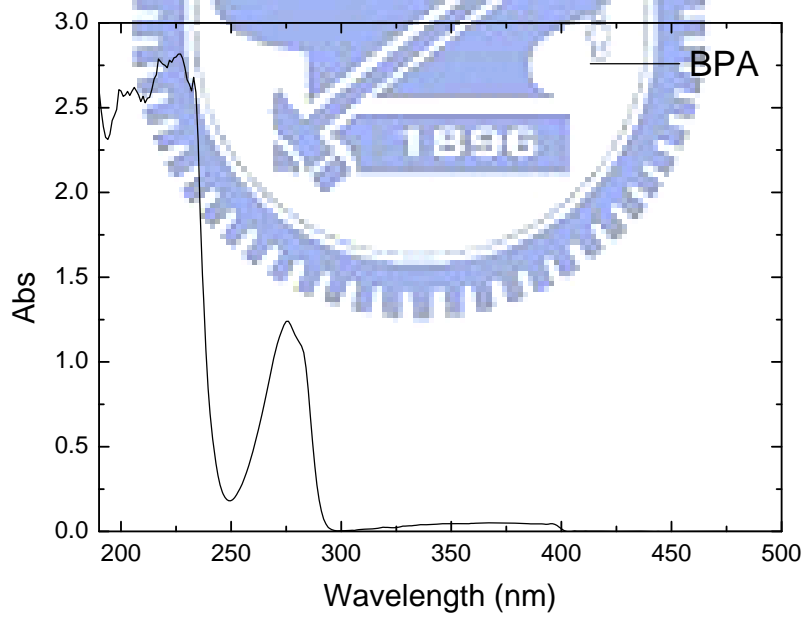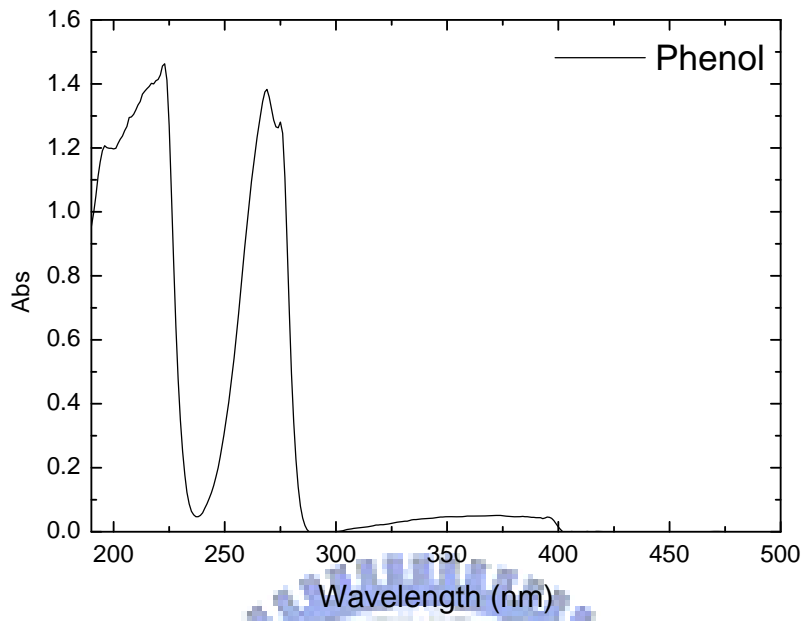| Measurement	Data mode	Starting wavelength	Ending wavelength	Sampling interval	Slit width	Reference
Wavelength scan	%R	800 nm	200 nm	1 nm	1 nm	Al_2O_3

Appendix A- 5   Operational parameters of TGA.

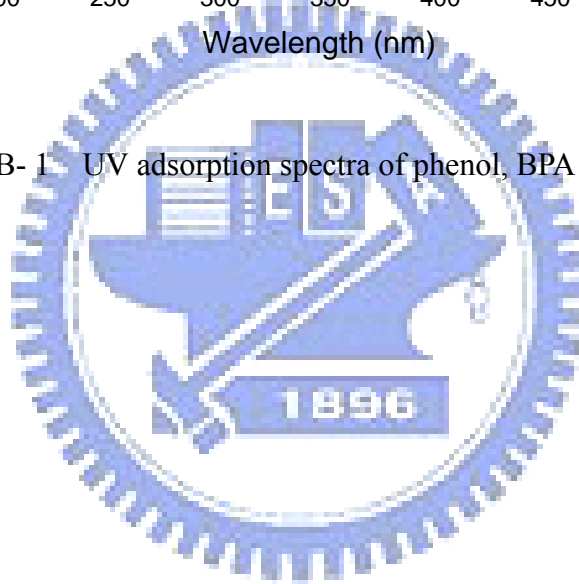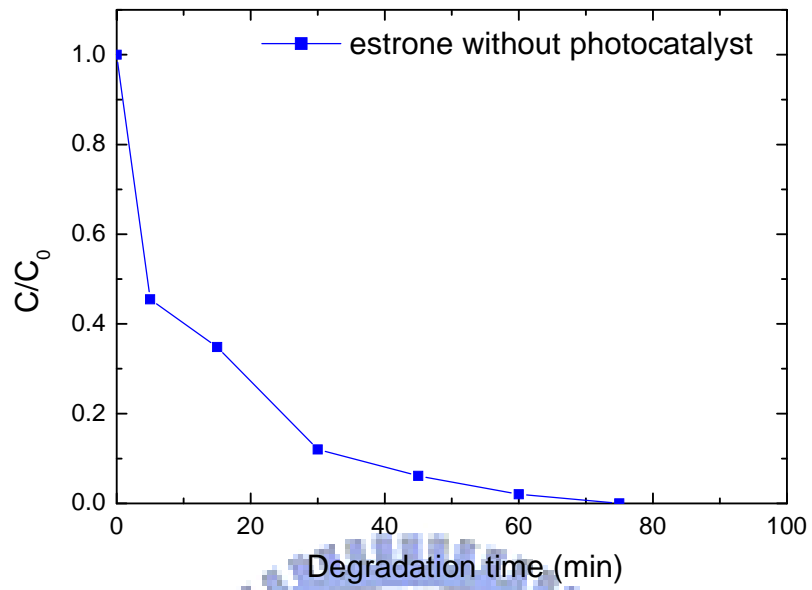| Starting temperature	Maximum temperature	Atmosphere	Heating rate ($°C$ /min)	Air flow rate (ml/min)
20 °C	900 °C	Air	10	20
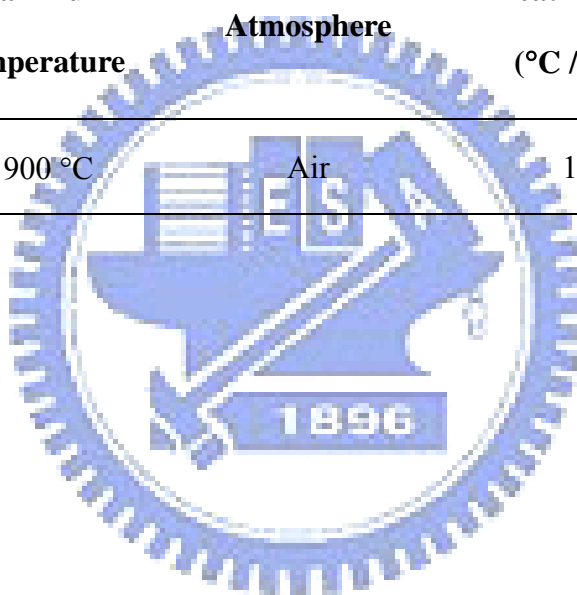
Appendix B.   Photocatalysis
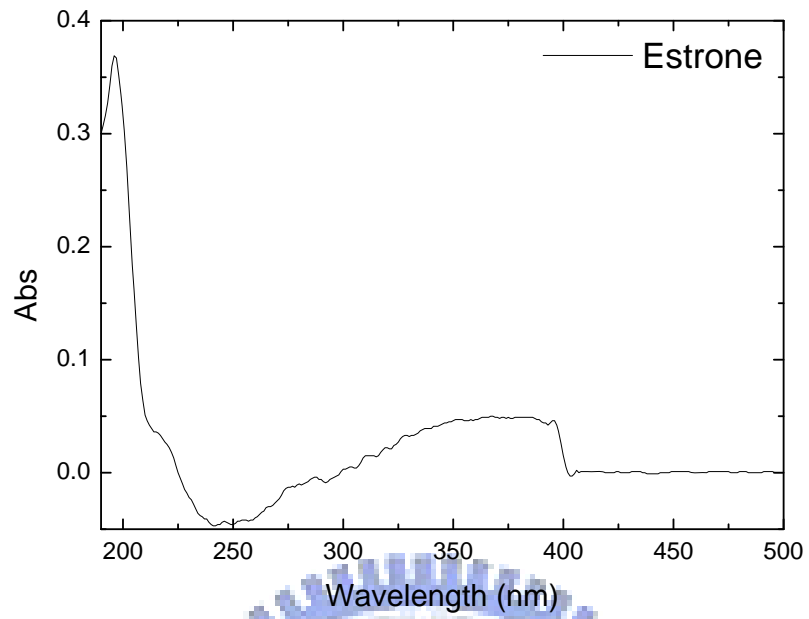
Appendix B- 1　　UV adsorption spectra of phenol, BPA and estrone.

Appendix B- 2   Time courses of photodecomposition of estrone without photocatalyst.